NOVA SCHOOL OF SCIENCE & TECHNOLOGY

DEPARTAMENTO CIÊNCIAS DOS MATERIAIS

David Manuel Seguro de Carvalho

Licenciado em Engenharia de Micro e Nanotecnologias

Fabrication of ultraviolet sensors based on ZTO and ZnO nanowires

MESTRADO EM ENGENHARIA DE MICRO E NANOTECNOLOGIAS

Universidade NOVA de Lisboa

março, 2023

DEPARTAMENTO DE CIÊNCIA DOS MATERIAIS

FABRICATION OF ULTRAVIOLET SENSORS BASED ON ZTO AND ZNO NANOWIRES

David Manuel Seguro de Carvalho
Licenciado em Engenharia de Micro e Nanotecnologias

Orientador: Dr. Joana Vaz Pinto, Auxiliary Professor, DCM, NOVA University Lisbon
Coorientador: Dr. Ana Rovisco, Postdoctoral Researcher, CENIMAT-i3N, NOVA University Lisbon

Júri:

Presidente: Dr. Pedro Miguel Cândido Barquinha
Arguente: Dr. Rui Alberto Garção Barreira do Nascimento Igreja
Vogal: Dr. Joana Vaz Pinto

MESTRADO EM ENGENHARIA DE MICRO E NANOTECNOLOGIAS

Universidade NOVA de Lisboa
março, 2023

Fabrication of ultraviolet sensors based on ZTO and ZnO nanowires.

Acknowledgements

Queria começar por agradecer ao Professor Rodrigo Martins e à Professora Elvira Fortunato (atual Ministra da Ciência, Tecnologia e Ensino Superior), fundadores do curso de Engenharia de Micro e Nanotecnologias, cujos percursos académicos abriram o caminho para que alunos como eu tivessem a oportunidade de se formarem em locais de investigação de excelência como é exemplo o i3N/CENIMAT e o CEMOP.

Às minhas orientadoras um obrigado muito especial. À professora Ana Rovisco que desde o primeiro até ao último dia, mesmo quando não lhe era possível, sempre se mostrou disponível e recetiva a ajudar-me em todas as vertentes que envolveram desenvolver esta tese. Desde a síntese nada fácil de $ZnSnO_3$, às sessões de SEM, a todos os esclarecimentos e sem esquecer a sua iniciativa ao propor-me a participação numa conferência. À Maria Morais, que só não foi minha orientadora em título, obrigado pela tua ajuda incansável. Obrigado pela tua ajuda nas mais diversas técnicas de caracterização e aos esclarecimentos de dúvidas que te trazia, onde só descansavas quando descobrisses uma solução. A tua forma de trabalhar e a tua solidariedade para com os outros são para mim fonte de grande inspiração. À professora Joana Pinto, uma das professoras com a qual mais aprendi ao longo do curso, muito obrigado. Obrigado pelo seu contributo na caracterização dos sensores e pelas nossas discussões sobre que rumo a tese deveria levar, onde abertamente discutimos ideias e onde me propôs novas formas de pensar. Queria lhe agradecer em especial por num momento mais delicado do meu percurso, onde você, numa breve conversa, muito provavelmente sem perceber, teve um papel determinante para que hoje eu esteja aqui a concluir o curso. Queria também agradecer à Barbara Domingos, colega que me acompanhou ao longo deste trabalho e que me deu a oportunidade de desenvolver este tema de tese.

Ao meu amigo de infância Filipe Sabino, amigo que me acompanhou neste curso, obrigado pela tua amizade. Através de ti consegui ver mais longe. Ao Eduardo Mata, aka Xang, amigo desde o berço, obrigado pelo teu apoio. Sempre estiveste ao meu lado, no melhor e no pior. Ao meu irmão rafeiro, Gonçalo Júlio, obrigado amigo. Desde as sandes quando eramos putos até aos cafés no Marinho. Daniel Costa, o verdadeiro militar que não quebra, obrigado. Sempre pronto para o que der e vier. Diogo Assis, o mais sábio dos sábios, obrigado, contigo aprendi muito. Francisco Rodrigues, amigo do peito, sempre foste uma referência, obrigado. Daniela Pereira, amiga de longa data, a nossa amizade é à prova de bala, obrigado.

Aos meus novos amigos, com quem travei amizade ao longo da tese, à Raquel, ao Guilherme, ao João, à Mariana, ao Pedro e ao Eduardo, obrigado por me terem acolhido e feito sentir à vontade neste meio da investigação.

Senhor Graciano, muito obrigado, foste muito importante no meu crescimento. Mais que um professor foste um amigo. Uma das tuas maiores lições foi o teu humor, que me ensinou como devemos encarar a vida. Estarás sempre comigo, obrigado.

À minha companheira, Mariana Moreira, obrigado por tudo. Sem a tua luz muito dificilmente teria chegado até aqui. O teu amor, carinho e cuidado levaram-me mais longe do que alguma vez quis ousar. Este feito é nosso, que se sigam os próximos.

Aos meus pais e irmão, palavras de agradecimento não são suficientes. Tudo fizeram para me proporcionar algo mais. Fizeram no por mim, sempre com o desejo de me fazer feliz. Espero um dia poder-vos retribuir. Obrigado pelo vosso amor incondicional. Aos meus avós, maternos e paternos, obrigado por tudo. Vocês são as raízes que tanto me orgulho. À restante família, não menos importante para alcançar esta meta, obrigado!

This work was financed by national funds from FCT – Fundação para a Ciência e Tecnologia, I.P., in the scope of the projects LA/P/0037/2020, UIDP/50025/2020 and UIDB/50025/2020 of the Associate Laboratory Institute of Nanostructures, Nanomodelling and Nanofabrication – i3N.

Resumo

A procura de novos materiais e respetivas técnicas de processamento que combinem melhores propriedades com um menor impacto ambiental é uma constante preocupação da comunidade científica. Sendo um dos grandes desafios melhorar o desempenho dos dispositivos através de práticas mais sustentáveis e ecológicas. Os óxidos metálicos, compreendendo os minerais mais abundantes na Terra, satisfazem estes requisitos com o seu leque variado de materiais. Particularmente os óxidos multicomponentes, tal como o óxido de zinco-estanho (ZTO), estão bem posicionados para responder às preocupações ambientais bem como para demonstrarem a sua relevância ao apresentarem uma vasta pluralidade de aplicações. Rovisco e um grupo de investigadores do i3N/CENIMAT reportaram recentemente pela primeira vez uma síntese hidrotérmica de nanofios de ZTO, a baixa temperatura (200 °C) e sem a utilização de sementes de crescimento, fornecendo assim uma via alternativa aos dispendiosos métodos de fase de vapor usualmente empregues. Estes nanofios foram estudados no i3N/CENIMAT e devido à sua natureza multifuncional já produziram resultados promissores na colheita de energia, integração em eletrónica e até mesmo em catálise. Neste trabalho, sensores de radiação ultravioleta (UV) utilizando nanofios de ZTO produzidos por solução, constituindo a camada ativa do sensor, são relatados pela primeira vez. Sensores UV atraem muita atenção devido às suas numerosas aplicações que abrangem várias áreas da indústria, da tecnologia e da vida quotidiana. Resumidamente a fabricação dos sensores consistiu na aplicação da técnica de *drop-casting* de uma solução de 4 µL de 800 nm de nanofios dispersos em álcool isopropílico (IPA) por cima da área dos *dedos* dos elétrodos interdigitais de Mo. Através de métodos simples de baixo custo e baixo consumo energético, os sensores UV foram obtidos mostrando uma boa resposta UV. Os sensores ZTO produzidos, quando irradiados com uma luz UV de 365 nm com uma potência de 2,6 mW, obtiveram um rácio de foto-corrente com a corrente no escuro (I_{ph}/I_{dark}) de 42 demonstrando uma responsividade (R_{UV}) de 6,4 µA/W. Utilizando técnicas de produção semelhantes, sensores UV baseados em ZnO, já intensivamente explorados na literatura, foram também fabricados e estudados para servirem como termo de comparação.

Palavras-chave: Sensores UV, óxidos metálicos, nanofios de $ZnSnO_3$, multifuncionalidade, nanofios de ZnO, síntese hidrotermal, sustentabilidade.

Abstract

The search for new materials and respective processing techniques that combine better properties with a lower environmental impact is a persisting concern in the scientific community, which not only wants to improve device performance but also wants to align itself with more sustainable and greener practices. Metal oxides, the most abundant minerals on Earth, meet these requirements with their diverse range of materials. Particularly, multicomponent oxides such as zinc-tin oxide (ZTO) are well positioned to address environmental concerns as well as to prove relevance by presenting a variety of applications. Rovisco and a group of researchers from i3N/CENIMAT recently reported for the first time a $ZnSnO_3$ nanowires (NWs) seed-layer free hydrothermal synthesis at low temperature (200 °C), providing an alternative route to the expensive high temperature vapor phase methods. These NWs have been studied and due to their multifunctionality nature, they have already produced promising results for energy harvesting, integration on electronics, and even catalysis. In this work, ultraviolet (UV) sensors using $ZnSnO_3$ solution-based NWs as the sensing material are reported for the first time. UV sensors have attracted a lot of interest recently due to their numerous applications covering various areas of industry, technology, and everyday life. The fabrication of the sensors briefly consisted of drop-casting a 4 µL solution of 800 nm length NWs dispersed on isopropyl alcohol (IPA) into to the finger area of Mo interdigitated-electrodes. Through simple low-cost and low-energy methods, UV sensors were obtained showing good UV response. The produced ZTO-based sensors obtained a photocurrent to darkcurrent ratio (I_{ph}/I_{dark}) of 42 when irradiated with a 365 nm UV light with a power of 2.6 mW, demonstrating a responsivity (R_{UV}) of 6.4 µA/W. Using similar production techniques, well-known ZnO-based UV sensors were also fabricated and studied to serve as a term of comparison.

Keywords: UV sensors**,** Metal oxides, $ZnSnO_3$ NWs, multifunctionality, ZnO NWs, hydrothermal synthesis, sustainability

Contents

List of Figures

List of Tables

Symbols

1D	one-dimensional
A_o	UV signal exposed area
$e^- - h^+$	electron-hole
E_g	bandgap
E_{LED}	LED radiation energy
E_x	free binding energy
h	Planck's constant (4.135×10^{-15} eV.s)
I_{dark}	darkcurrent
I_{ph}	photocurrent
I_{ph}/I_{dark}	photocurrent to darkcurrent ratio
ΔI	response current
P_{UV}	UV illumination Power
R_{UV}	responsivity
S_{UV}	sensitivity
t_{fall}	fall time
t_{rise}	rise time
$\bar{l} / \bar{d}$	average Length/Width
V	voltage
V_B	valence band
C_B	conduction band
$V_O^{\bullet}$	ionized oxygen vacancy
V_O	oxygen vacancy

$\mathbf{V_{Zn}}$	zinc vacancy
$\mathbf{O_i}$	interstitial oxygen
$\mathbf{O_{Zn}}$	oxygen atom at the zinc position in the crystal lattice
$\mathbf{Zn_i}$	interstitial zinc
$\mathbf{Zn_O}$	zinc atom at the oxygen position in the crystal lattice
$\boldsymbol{\lambda}$	wavelength of electromagnetic wave
$\boldsymbol{\nu}$	Frequency of electromagnetic wave
$\boldsymbol{\Phi_B}$	built-in electric field

Abbreviations

CENIMAT	Centro de Investigação de Materiais
i3N	Associate Laboratory Institute of Nanostructures, Nanomodelling and Nanofabrication
Fcc	face-centered cubic
IPA	isopropyl alcohol
I-V	current-voltage
K-M	Kubelka-Munk
LED	light-emitting diode
MW	microwave
NWs	nanowires
Orth	Orthorhombic
PL	photoluminescence
PR	photoresist
R	reflectance
RF/DC	radio frequency/direct current
SEM	scanning electron microscopy
UV	ultraviolet
XRD	X-ray diffraction
ZnO	zinc oxide
ZTO	zinc-tin oxide

Motivation and Objectives

Recently a team of researchers from i3N/CENIMAT has developed a low-temperature hydrothermal synthesis of $ZnSnO_3$ NWs that has shown to be promising. These NWs have demonstrated their multifunctional potential in applications such as energy harvesting, integration in electronics and in photocatalysis. It should be noted that $ZnSnO_3$ NWs synthesized via solution-based methods have not yet been reported in the literature for their use in UV sensing applications. Furthermore, regardless of the production method and the nanostructures type, very little research has been done in UV sensing field using ZTO. Therefore, the main motivation is to study the properties and potentiality of these $ZnSnO_3$ NWs in the detection of UV light. The opportunity to contribute to an i3N/CENIMAT research project while exploring new directions provided great motivation for this work

With these goals outlined, it was intended that the fabrication of $ZnSnO_3$-based UV sensors, from the nanostructures synthesis to the fabrication of the sensor itself, was developed allying simple, inexpensive fabrication techniques with low-cost and environmentally friendly materials.

Another objective was to characterize as completely as possible the fabricated UV sensors. To this end, it was deemed necessary to produce and characterize UV sensors based on another metal oxide, also in the form of NWs and also produced by solution – the well-known ZnO. Given that this material has already been intensively explored for this application, it was considered that it could serve to better understand the results of $ZnSnO_3$-based UV sensors - in turn a material very little used in this application.

The characterization of the sensors aimed to better understand the UV response not only through the structural, morphological, and optical characterization of their nanostructures but also through the electrical characterization of the devices, where it is pretended to study the effect of:

- Applied bias voltage;
- Finger spacing of the sensor's interdigital configuration;
- Power of the UV light.

In an attempt to fulfill these objectives and aiming at a better understanding of the nanostructures UV response, the final objective is to propose new strategies that may improve the performance of these devices.

Outputs:

During the development of this thesis, I had the opportunity to participate in an international conference, the RSC Chemical Nanoscience and Nanotechnology Early Career Researcher Virtual Poster Meeting, on June 20, 2022. At the conference, I presented part of this work on the development of ZnO-based UV sensors, with a focus on the methods and techniques used in their fabrication. As a first-time attendee at an international conference, I participated in productive discussions with other scientists and researchers on my work and the work of others presented at the conference. This exchange of ideas proved to be highly enriching. In recognition of my work, I was awarded **Best Poster** in the Techniques category.

Here is the previously mentioned output:

Posters:

David Carvalho, [a] Ana Rovisco, [a] Maria Morais, [a] Elvira Fortunato, [a] Rodrigo Martins, [a] Pedro Barquinha, [a] and Joana Vaz Pinto, [a], Low-cost UV sensors based on solution processed ZnO microrods, RSC Chemical Nanoscience and Nanotechnology Early Career Researcher Virtual Poster Meeting, 20th of June 2022.

Additionally, the work presented in this thesis is being prepared in the format of a manuscript to be submitted to a scientific journal.

1 Introduction

Metal oxide nanostructures have attracted immense interest due to their unique optical and electrical properties as well as their promising applications in the fabrication of nanodevices [1]. Especially, semiconducting metal oxides like ZnO, TiO_2, and SnO_2 have been investigated and widely used because of their properties, which have rendered them suitable for widespread applications in energy conversion, catalyst, and sensing [2].

As a typical class of ternary oxides, zinc stannate ($ZnSnO_3$ and Zn_2SnO_4), which is generally called zinc tin oxide (ZTO), has received much attention because of its high electron mobility, high electron conductivity, attractive optical properties as well as good stability compared to its binary counterparts (ZnO and SnO_2) [3]. This type of multicomponent oxides also demonstrates the ability to manifest different properties by adjusting the cationic ratio, resulting in a wider range of applications for a given material system, making this kind of material very versatile [4]. Although, due to its multicomponent nature, the synthesis is far more complex than its binary counterparts [5]. Notwithstanding this obstacle, Rovisco *et al*. developed a method to synthesize $ZnSnO_3$ NWs through a low temperature and seed-layer free hydrothermal synthesis [4,5]. In this thesis, it is proposed to explore one of the many potentialities of the multifunctional $ZnSnO_3$ in the application of ultraviolet (UV) irradiation detection comparing its performance to the well-established ZnO.

1.1 Metal Oxide Nanowires for UV Sensing Application

UV sensors have drawn a significant amount of attention because of the numerous applications they have in the industry, technology, and daily life [6]. Some of these are notable for daily living in terms of sun/UV irradiation exposure that may cause different types of diseases including cataracts, skin cancer, etc., thus, it is suggested that a modern and effective UV sensor be developed allying simple, inexpensive fabrication techniques with low-cost and environmentally friendly materials [7]. Moreover, these applications include ones for environmental safety, medicine, military defense, flame detection, environmental sensors, and space communication [8].

The four spectral regions of UV light that are typically distinguished are UV-A (for wavelengths between 400 nm and 320 nm), UV-B (for wavelengths between 320 nm and 280 nm), UV-C (for wavelengths between 280 nm and 200 nm), and far UV (for wavelengths between 200 nm and 10 nm, which reaches the X-ray spectral low energy frontier), where the UV-A band's content in the solar spectrum is higher than that of the UV-B, UV-C and far UV bands [6,9]. Figure 1.1 shows this UV light categorization.

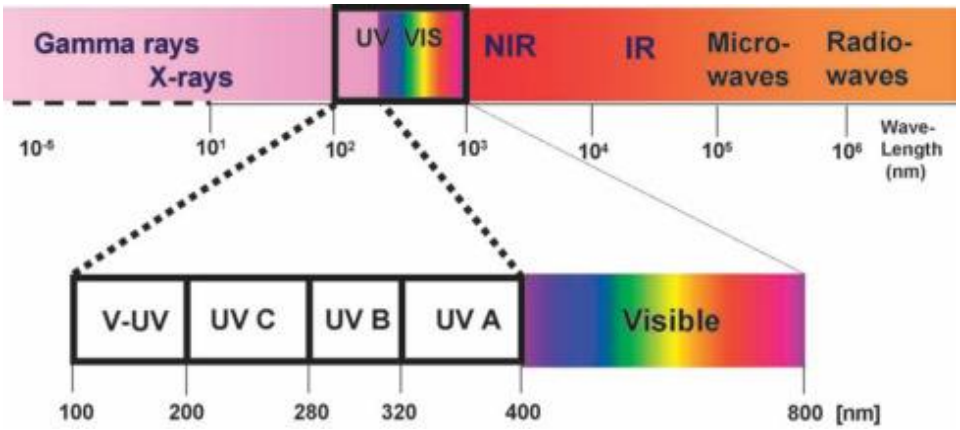

Figure 1.1: Electromagnetic energy spectrum highlighting the UV classification (image adopted from [9]).

The working mechanism for UV sensors is mainly based on the photoconductivity effect, wherein, in the presence of UV illumination, wide bandgap semiconductors absorb UV light and produce electron-hole (e^- - h^+) pairs when the photon energy ($h\nu$) is greater than or equal to the bandgap (E_g). The photogenerated electrons and holes are then collected in the external circuit as a photocurrent. Therefore, the photoconduction process primarily involves three steps: i) UV radiation is absorbed, creating e^- - h^+ pairs; ii) these photogenerated pairs are then separated through a transportation process; and finally, iii) photogenerated electrons and holes are collected as photocurrent [7].

Since they are the most abundant minerals on earth, metal oxide materials are the focus of current research in nanotechnology areas such as transparent electronics, piezoelectric transducers, catalysis, sensors, and electro-optical and electro-chromic devices [10].

In-depth research has been done on one-dimensional (1D) metal oxide nanostructures for the fabrication of nanoscale sensors [11]. 1D structured materials are sized at the nanoscale level in two dimensions and include nanotube, nanofiber and NW structures, to name a few [12]. Because of their small size, nanostructures can exhibit new and significantly modified physiological, chemical, and biological properties that differ from those of the micrometric scale [10]. 1D metal-oxide nanostructures have several advantages over traditional film sensors such as bulk and thin film materials. Particularly, a higher surface-to-volume ratio with carrier and photon confinement in two dimensions, larger Debye length comparable to their small size and superior stability due to their high crystallinity [10,13].

In particular, on metal oxide NWs, the large surface-to-volume ratio and the presence of deep-level surface trap states increase the lifetime of the photocarrier while the reduced dimensionality of their active area in the devices shortens the carrier's transit time [14].

1.2 Metal Oxide UV sensing mechanism

The most widely accepted UV sensing mechanism for metal oxide materials, despite being a contentious subject, is the result of a change in the electrical conductivity or resistivity of the semiconductor due to the adsorption and desorption of oxygen-rich molecules [8,15]. Usually, a ZnO NW is used as a model to describe this mechanism [7,16].

In the dark, the ZnO surface is always partially covered by adsorbed oxygen molecules, which tend to bond particularly at surface oxygen vacancies and trap electrons from the conduction band (C_B). This process produces an upward band bending at the surface as well as a corresponding depletion region. As illustrated in Figure 1.2 (a), when the UV light is turned on, the initial band bending quickly separates the photogenerated carriers, sweeping the holes toward the surface while keeping the electrons in the NWs' inner part. Because of this separation, the probability of carrier recombination is lower, and the lifetime of electrons in the C_B increases. Thus, photoconductivity rises extremely fast at first. After some time, the photogenerated holes localized at the surface can induce oxygen desorption from the NWs' surface by recombining with the trapped electrons. As a result of this process, the concentration of electrons previously trapped at the surface decreases, and consequently the height of the upward band bending decreases as well, as it is illustrated in Figure 1.2 (b). As the built-in electric field (Φ_B) (caused by the band bending) decreases, the probability of electrons from the C_B overcoming it and reaching the surface increases. As a result, some of the electrons may become trapped again, promoting the process of oxygen readsorption. After a while, the photocurrent saturates as an equilibrium between the desorption and readsorption rates is reached [16].

When the incident UV light is turned off, the electrons and holes recombine rapidly, and the device attempts to return to its original state.

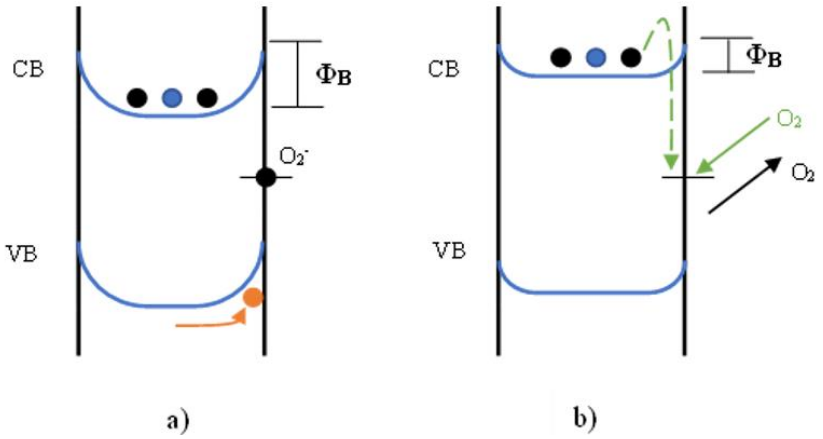

Figure 1.2: (a) The photogenerated electrons and holes in a ZnO nanowire are separated by the built-in electric field (Φ_B) caused by the band bending; (b) The energy barrier at the surface decreases as the excitation process continues, allowing oxygen molecules to readsorb. As a result, the photocurrent saturates when an equilibrium between desorption and readsorption is reached. In both figures, the color of photogenerated-carriers is blue, whereas other electrons in the conduction band determine the intrinsic n-type conductivity of ZnO and are indicated in black. The green arrows describe the retrapping of electrons and the oxygen readsorption. Schematic adapted from [16].

1.3 Solution-based ZnO main properties as UV sensor

For several years, ZnO has received a lot of attention due to its distinct properties and potential use in electronic and optoelectronic devices [17]. ZnO is currently widely used in many different applications, including transparent conductive oxide, solar cells, gas sensors, chemical and biological sensors, piezoelectric transducers, lasers, light-emitting diodes, and UV detectors [18]. However, UV sensing is one of the most researched applications for ZnO due to its high sensitivity and selectivity and ability to absorb UV light [19].

From a broad list of functional materials, ZnO is an II-VI-group n-type semiconductor material with a *Eg* (≈3.37 eV) that crystallizes in a hexagonal wurtzite structure [20]. This metal oxide material has high chemical stability, strong radiation hardness, a wide range of electrical conductivity ranging from 10^{-9} to 10^{4} $\Omega \cdot cm^{-1}$, it is abundant (with a non-toxic nature) and is simple to manufacture [11,17,21]. Furthermore, the exciton binding energy of ZnO is 60 meV, which is much higher than the thermal ionization energy (26 meV) at room temperature. As a result, its excitons can remain stable at room temperature, ensuring efficient exciton emission at low excitation energy [22]. It is as well added that, pure ZnO is also highly transparent in the visible and near-infrared ranges of the electromagnetic spectrum [20].

Microwave hydrothermal synthesis is particularly interesting among the existing methods for obtaining ZnO structures because of the high reaction rates caused by microwave radiation absorption by the materials which allows reactions to be completed in minutes [15,23].

Singh *et al.* [24] reported the UV photoresponse of ZnO nanorods grown hydrothermally with the aid of a seed-layer, using low-energy and cost-effective techniques. Additionally, the sensor was fabricated with the same interdigitated electrode configuration, with palladium electrodes deposited onto the nanorods. The device demonstrated a photocurrent of 1.29×10^{-4} A, a photocurrent to dark current ratio of approximately 2, and a responsivity of 0.19 $A \cdot W^{-1}$.

Through more complex and high-temperature methods, Mallampati *et al.* [25] reported on the performance of ZnO NW-based UV sensors. The ZnO NWs were synthesized through self-catalyzed growth at 800 °C. The NWs were transferred onto a quartz substrate and aluminum contacts were deposited before annealing the device at 250 °C. Despite the prolonged response time of several minutes, the device exhibited a photocurrent in the hundreds of nA and a remarkably high responsivity on the order of 10^{5} A·W. Alsultany

et al. [26] fabricated a UV sensor with an interdigitated electrode configuration based on catalyst-free growth of ZnO nanowire using high-temperature methods such as RF/DC sputtering and an annealing at 450 °C. The device exhibited a photocurrent of 1.79 $\times 10^{-4}$ A, a photocurrent to dark current ratio of 24.2, and a responsivity of 0.39 $A \cdot W^{-1}$. Moreover, the response and recovery times of the device were calculated to be 3.9 and 2.6 s, respectively.

1.4 Solution-based $ZnSnO_3$ NWs main properties as UV sensor

The demand for low-cost materials/methods has increased significantly. Zinc-tin oxide (ZTO) appears to be an ideal candidate for several applications due to its high electrical conductivity, mobility, and lack of critical raw materials. The multicomponent nature, together with the wide range of different ZTO nanostructures provide this material system with truly impressive multifunctionality [27,28].

ZTO can exist in two crystalline structures depending on the molar ratios of the primary components (Zn, Sn, and O): the stable phase, Zn_2SnO_4, which is an orthostannate with an inverse spinel structure, and the metastable phase, $ZnSnO_3$, which can have a rhombohedral structure or a perovskite structure, either orthorhombic (orth) or ordered face-centered structure (fcc) [28,29]. The excellent properties of $ZnSnO_3$ such as its relatively low crystallization temperature, wide bandgap, and high transmittance in the visible region, make it an especially valuable material to use in optoelectronic devices. $ZnSnO_3$ is an n-type semiconducting metal oxide with an optical E_g ranging from 3.6 to 3.9 eV; this means that ZTO can be used as a conducting material in optoelectronic devices [30,31]. In addition, compared to SnO_2 and ZnO, $ZnSnO_3$ is more thermally and chemically stable in ambient conditions [30].

Fundamentally, vapor-phase methods have been used to produce $ZnSnO_3$ NWs, because, due to the higher temperatures of the former, methods such as chemical vapor deposition and thermal evaporation are more efficient. However, these techniques are expensive and require high temperatures (> 700 °C) [27]. In contrast, $ZnSnO_3$ NWs produced through a low temperature (200 °C) hydrothermal synthesis were for the first time used in this research as the photosensitive material to detect UV radiation. This technique, which is low-cost and simple but still enables well-control and highly reproducibility, offers an excellent alternative to conventional physical methods [4,5]. These $ZnSnO_3$ NWs were already employed as photocatalysis [32], energy harvesters [33] and electronics, demonstrating really good results.

Since $ZnSnO_3$ is a metastable phase, and is harder to produce, it has received less attention than Zn_2SnO_4, a more stable phase. The orthostannate phase has already been vastly investigated for UV detection [34–36]. On the other hand, there are only few reports on the use of $ZnSnO_3$ as UV sensor.

Xue *et al.* [37] demonstrated the UV response of a single $ZnSnO_3$ NW positioned between two Au electrodes with a 300 nm spacing. These NWs were synthesized by thermal evaporation and showed a darkcurrent of 0.3 nA and a photocurrent of 162 nA. Besides, on the UV cycles graphics it was possible to verify that the photocurrent oscillated between a large interval of current values.

Wang *et al.* [38] reported the fabrication of UV sensor by employing $ZnSnO_3$ cubic nanoparticles as the active material. The device fabrication process consisted of spin-coating a hydrothermally synthesized $ZnSn(OH)_6$ solution on a ceramic substrate with Au interdigitated electrodes. After that, the film was annealed at 500 °C to obtain $ZnSnO_3$. Through the use of an expensive material like Au and a complex and high temperature technique, the nanocubes responded well to UV, with a photocurrent to darkcurrent ratio of approximately 8×10^3 and rise and fall times of 20 and 59 s, respectively. Nevertheless, it is not clear that the measured photocurrent had enough time to stabilize, appearing that would decrease if it had.

To conclude, this project aims to overcome the lack of ZTO NWs produced by solution-based methods and to acquire a better understanding of their properties and potential as the active material of UV

sensors. As a result, this project reports for the first time the use of $ZnSnO_3$ solution-based NWs in the detection of UV irradiation. As a starting point and benchmark, ZnO-based UV sensors produced with analogous techniques were also studied and characterized.

1.5 Characteristic Parameters of UV sensors

A variety of parameters that characterize a device's behavior are typically used to describe its performance. In this sense, this subchapter outlines some of the most relevant parameters in describing the operation of a UV sensor.

The current formed in the external circuit, when the sensor is being irradiated with UV light, is known as *Photocurrent* (I_{ph}). Per opposition, the current that remains in the detector in the absence of UV radiation is called *Darkcurrent* (I_{dark}) [11].

The current produced by the sensor under UV illumination is referred to as the sensor *response current* (ΔI), from which the current produced only by UV can be distinguished [7]. The ΔI is thus defined by the difference between I_{ph} and I_{dark} [15]:

$$\Delta I = I_{ph} - I_{dark} \tag{1}$$

Moreover, the *responsivity* (R_{UV}) of a sensor is another important parameter that provides information about the generation of ΔI per unit incident UV illumination Power (P_{UV}) on a sensor4 and can be expressed by the following equation [19,39]:

$$R_{UV} = \frac{\Delta I}{P_{UV}} = \frac{\Delta I}{P A_o} \tag{2}$$

where P is the power of the UV signal per unit of area and A_o the UV signal exposed area.

The ratio of I_{ph} to I_{dark} (I_{ph}/I_{dark}) is another parameter that is frequently used to describe the performance of UV sensors. However, the term used for this parameter has not been agreed upon in the literature. This parameter provides information about the signal-to-noise ratio for a given UV intensity, and whatever name it goes by, it is a parameter that is widely used in the literature to compare the performance of UV sensors [7]. This ratio is referred in the literature as *Sensitivity* [7,8] *photosensitivity* [40], or even *Gain* [41]. In this thesis, this current ratio will be referred as simply by I_{ph}/I_{dark} so the parameter *Sensitivity* assumes a physical meaning according to a broader definition that the term *Sensitivity* usually adopts in the sensor field. *Sensitivity* is more often acknowledged as the minimum input change required to produce a measurable unit change in the output [42]. In this context the input is the P_{UV} and the output the ΔI. If the sensor response to UV light is non-linear, *Sensitivity* will vary over the sensor range and can be found by calculating the derivative of ΔI with respect to P_{UV} $\left(\frac{d\Delta I}{dP_{UV}}\right)$ [42]. The mathematical relation of the *Sensitivity* (S_{UV}) is represented on the following equation:

$$S_{UV} = \frac{d\Delta I}{dP_{UV}} \tag{3}$$

The speed with which a photodetector responds to UV is another important characteristic features and is defined by how quickly a sensor detects a UV signal or returns to its original state after switching off the UV [7]. The photodetection speed of a UV sensor is mainly determined by two parameters: rise time (t_{rise}) and fall time (t_{fall}), which correspond to the time needed between 10 % and 90 % of the maximum I_{ph} and the time that elapses between 90 % and 10 % in the absence of UV light, respectively [15].

2 Materials and Methods

In this section it is described the techniques and procedures employed in this thesis work from the hydrothermal synthesis of ZnO and ZTO structures to their respective characterization techniques. Here are also described the fabrication methods performed to produce the UV sensors based on both previously mentioned materials, using as a model device an interdigitated electrode configuration. Finally, the electrical characterization of both ZnO and ZTO-based UV sensors is also detailed.

2.1 ZnO synthesis

The ZnO NW´s were produced through a hydrothermal synthesis assisted by microwave (MW) irradiation, as described in reference [43]. Essentially, 20 mL of deionized water were used to dissolve 2.2 g of zinc acetate dihydrate from Alfa Aesar, and the solution was then stirred. Then after, 6.4 g of sodium hydroxide (LABKEM) was added to the previous solution. A surfactant solution was prepared by mixing 50 mL of deionized water with 40 mg of sodium dodecyl sulphate (Sigma-Aldrich). The synthesis was carried out in a 35 mL Pyrex vessel by mixing 2 mL of the first solution, 5 mL of surfactant solution, and 10 mL of deionized water, which was then loaded into a CEM corporation Discovery SP microwave. The exposure condition was 100 W of microwave radiation for 5 min. The vessel was cooled to room temperature after the reaction. The white precipitates were then centrifuged three times at 4500 rpm with de-ionized water followed by isopropyl alcohol alternately, using a Neya 16 centrifuge (Remi). Finally, the powders were dried for 3 hours in a vacuum desiccator (SELECTA) at 60 °C.

2.2 ZTO synthesis

The $ZnSnO_3$ NWs synthesis was based on the method developed by Rovisco *et al.*, which consists of a hydrothermal synthesis at lower temperature not requiring a seed layer to induce the NWs' growth [4,5]. The hydrothermal method was performed in a conventional oven using tin (IV) chloride 5-hydrate $SnCl_4.5H_2O$ (0.01 M/0.1050 g) from Riedel-de Haën and zinc chloride $ZnCl_2$ (0.02 M/0.0818 g) from Merck, as tin and zinc precursors, respectively. As the mineralizer sodium hydroxide, NaOH (0.24 M/0.1450 g) from Sigma-Aldrich was used. The solvents employed were deionized water and the surfactant ethylenediamine (EDA) from Sigma-Aldrich in a volume proportion of 7.5:7.5 mL.

First both zinc and tin precursors were milled and then dissolved separately in 7.5 mL of deionized water at constant stirring being then mixed together. Subsequently, 7.5 mL of the surfactant were added to the previous solution which was then left stirring for 30 min. Following that reaction time, the mineralizer was previously milled and then added to the main solution. The resulting solution was transferred into a 45 mL Teflon-lined stainless-steel autoclave (Parr Acid Digestion Bombs, no 4744) and kept in an electric oven (Thermo Scientific) at 200 °C for 24 h, using a heating ramp of 200 °C·h^{-1}. The white precipitate that arises from the oven was then washed by being centrifuged at 6000 rpm with deionized water and isopropyl alcohol 5 times alternately, using a Neya 16 centrifuge (Remi). Finally, the nanostructures precipitate was dried in a vacuum desiccator (SELECTA) at 60 °C for 2 h in vacuum.

2.3 Nanostructures Characterization

To determine the crystallographic structure of both materials X-ray diffraction (XRD) was performed using a PANalytical's X'Pert PRO MRD diffractometer with CuKα radiation source (wavelength 1.540598 Å). The XRD data was acquired in the 20 – 80 ° 2θ range with a step size of 0.016 °, in Bragg-Brentano configuration.

Raman spectroscopy measurements were achieved in a Renishaw inVia Reflex micro-Raman spectrometer with an obtained spectra ranging from 5 to 1790 nm.

The photoluminescence (PL) measurements were performed at room temperature, using a PerkinElmer LS.55 instrument with a Xenon lamp as excitation source with an excitation wavelength of 350 nm.

Optical characterization was performed using a PerkinElmer lambda 950 UV/VIS/NIR spectrophotometer. The reflectance spectra were acquired between 250 and 800 nm and the method used to calculate the optical band gap was the Kubelka-Munk (K-M) method.

To investigate the synthesized structures morphology, a scanning electron microscopy (SEM) with a Carl Zeiss AURIGA CrossBeam Workstation was used.

2.4 UV sensor device fabrication

The interdigitated electrodes were deposited by sputtering a molybdenum (Mo) layer of 70 nm thick on top of a previously cleaned glass substrate (Corning Eagle XG Glass: 100mmx100mmx1.1mm). The sputter deposition conditions were: DC power of 175 W, Ar flow of 40 sccm, and 0.24 Pa of deposition pressure. The electrodes were subsequently patterned by photolithography. Spin-coating was used to evenly spread the photoresist (PR), then the PR was patterned, and finally a reactive-ion etching was performed in an SF_6 atmosphere (Power of 50 W, pressure of 3.99 Pa, for 120 s). In a 10 by 10 cm glass several electrodes are arranged in rows with a spacing between fingers of 50 µm, 30 µm and 10 µm.

After the fabrication of the interdigitated electrodes, a series of steps were taken in order to build the UV sensor device, as shown in a schematic presented in Figure 2.1 and also in Annex A. First of all, a Kapton mask was placed over the electrodes to leave only the finger area uncovered, thus preparing for the subsequent drop-casting of the active material in this area. The mask was made by laser cutting a square in a Kapton tape (Farnell) with exactly the same area as the finger area, using a Universal Laser System VLS3.50. After applying the mask, the surface of the electrodes received a UV/ozone treatment. This treatment allowed the surface to become more hydrophilic, enabling the drop to spread evenly over the finger area. To perform the UV/ozone treatment the electrodes were placed 6 cm from the UV lamp for 5 min. This treatment was only performed for the ZnO-based UV sensors since in the case of the ZTO sensors, the drop of this material spread more easily, filling the desired area without the need for this treatment. The drop quantity was optimized to use the least amount of drop that completely filled the finger area without overflowing it. The goal was to create the most reproducible sensor and homogeneous film possible using the drop-casting method. Then a 9 µL drop for the ZnO sensors and a 4 µL for the ZTO sensors with both nanostructures dispersed in isopropyl alcohol (with a concentration of 10 mg/mL for both ZnO and ZTO structures) was dropped on the finger area using the technique drop-casting. After evaporating the solvent on a hot plate at 70 ºC for 2 min, a film was formed, and the sensor was completed as depicted in Figure 2.2 and in Annex B.

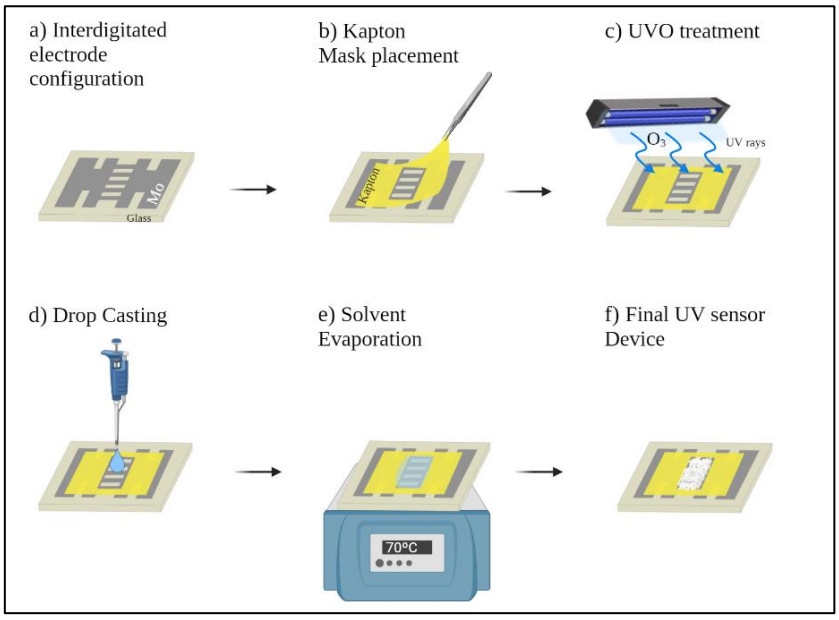

Figure 2.2: Process flow for the fabrication of UV sensors, depicting the sequential steps involved in the fabrication process

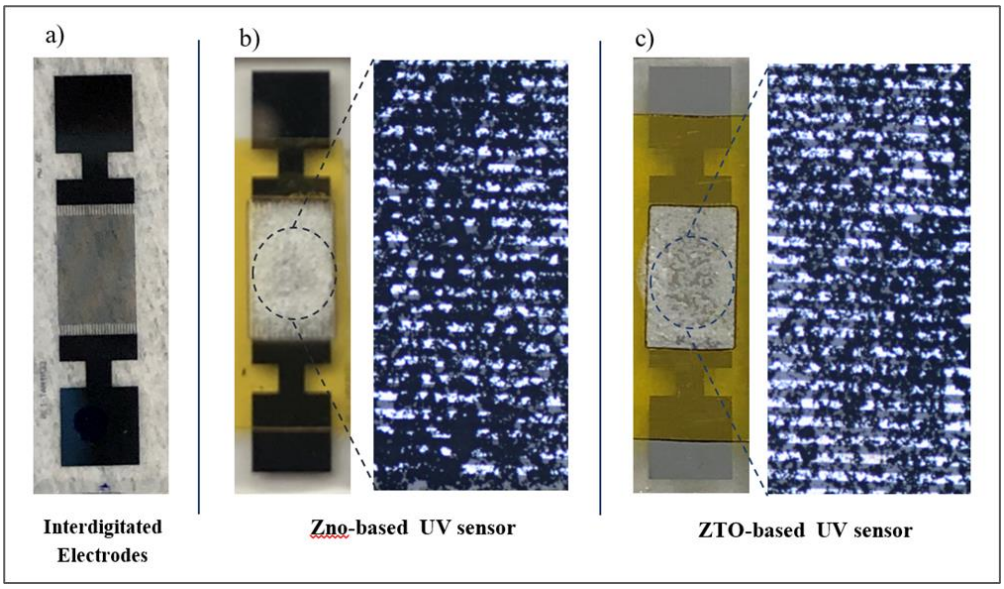

Figure 2.1: a) Image of the Mo interdigitated electrode configuration used to fabricate UV sensors. b) Image of a ZnO-based UV sensor, with a magnified view of the central region of the finger area where ZnO NWs are dispersed. c) Image of a ZTO-based UV sensor, with a magnified view of the central region of the finger area where ZTO NWs are dispersed.

2.5 Electrical Characterization

The electrical characterization of the UV sensors was performed in, a semiconductor parameter analyzer (Agilent 4155C from Keysight Technologies) and using an Everbeing probe station (Everbeing Int'l Corp.) .The devices were exposed to UV light at 365 nm and with a maximum 4.7 mW of P_{UV}. For this purpose, a fiber coupled UV LED (M365F1, Thorlabs Inc.) operated by a Thorlabs DC4100 controller (Thorlabs Inc.), and a pulse generator (Pulse Pal, Sanworks LLC) - programmed to turn the UV LED on and off at specified time intervals - were employed. The UV LED was positioned on top of the sensors in order to concentrate the light in its active area, where the nanostructures were dispersed. The measurements made consisted of on/off cycles where the sensors where exposed to 500 s of UV light followed by 500 s in the dark. During the cycles the tests were conducted for different applied voltages (1, 5 and 10 V) and also for different P_{UV}´s (0.05, 0.70, 1.70, 2.60, 3.50, 4.50 and 4.70 mW).

3 Results

This chapter presents and discusses the results obtained throughout this thesis' work. It is proposed to explain and understand the operation of the fabricated devices - UV sensors, through the characterization of the nanostructures that act as the active material in the detection of UV light, together with the electrical characterization of the devices themselves, by correlating theoretical concepts and results previously obtained by other researcher groups.

Subchapters 3.1 and 3.2 are dedicated to the structural, morphological, and optical characterization of hydrothermally synthesized nanostructures, explicitly ZnO and $ZnSnO_3$ NWs.

3.1 Synthesized ZnO NWs Characterization (structural, morphological, and optical)

XRD and SEM analyzes were performed to determine the crystallographic structure and morphology of the synthesized ZnO NWs. Figure 3.1 depicts the XRD diffractograms of ZnO NWs. The observed peaks are totally correlated with the hexagonal wurtzite ZnO structure (ICDD 36-1451), with no evidence of other phases being present.

To evaluate the crystallite size of the NWs Scherrer's equation was used:

$$\tau = \frac{k\lambda}{\beta cos\theta}, \tag{4}$$

where τ is the crystallite size (nm), k is the Scherrer constant, λ is the wavelength of the X-ray radiation (Cu-K_α = 0.1541 nm), β is the full width at half maximum (FWHM) of the intense and broad peaks and θ is the Bragg's diffraction angle of the peak [44].

The three main peaks corresponding to the crystallographic planes (100), (002) and (101) were used to apply the Scherrer formula, and the average result was a crystallite size of 55.8 nm.

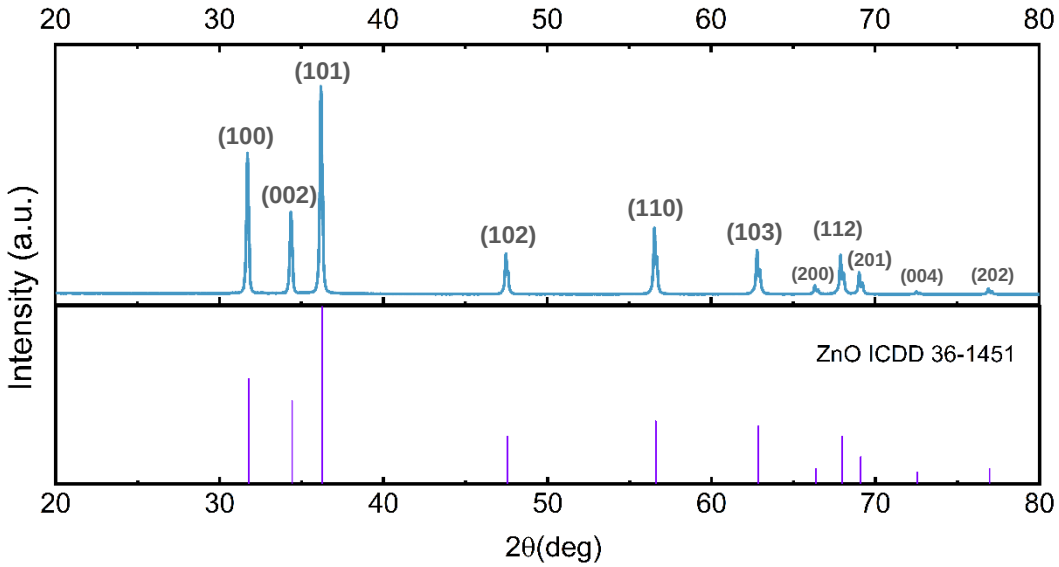

Figure 3.1: XRD diffractograms of the ZnO NWs synthesized via hydrothermal synthesis assisted by MW and the reference used for ZnO (ICDD 36-1451).

Raman spectroscopy was used to examine the synthesized ZnO NWs optical characteristics, and the results are shown in Figure 3.2. ZnO with a wurtzite structure belongs to the C_{6v}^4 (P63 mc) space group. Considering a perfect ZnO crystal, only the lattice optical phonons at Γ point of the Brillouin zone are involved in first-order Raman scattering [43]. The following optical modes are predicted to exist in the group theory: Γ = A_1 + 2B_1 + E_1 + 2E_2 [45]. The active Raman modes include the modes A_1, E_1, and E_2, with A_1 and E_1 also being infrared active and divided into longitudinal–optical (LO) and transversal–optical (TO) components [46]. E_2 mode is composed of two modes, a low and a high-frequency phonon ($E_2^{low}$and E_2^{high}), which correspond to the vibration of the heavy Zn sublattice and oxygen atoms, respectively. For the B_1 mode, it is silent and has two frequencies which are the B_1^{low} and B_1^{high} mode [45].

Raman spectra in Figure 3.2 show the two most intense peaks located at 100 and 438 cm^{-1} and are attributed to the E_2^{high} and E_2^{low} optical modes, respectively, which are characteristic of the wurtzite hexagonal of ZnO [47].The small peak at 330 cm^{-1} is assigned to the E_2^{high}- E_2^{low} (multiphonon process) and is known to be a second order vibration mode caused by zone-boundary phonons [43]. The broad peaks at 663 and 1150 cm^{-1} are also consistent with the multiphonon process [45]. The peak at 385 cm^{-1} is attributed to the A_1(TO) mode, and the peak position at 208 cm^{-1} is attributed to the second-order $2E_2^{low}$ structure [47]. The B_1^{low} silent mode, which is activated by the formation of defects in the ZnO structure, is responsible for the small broad peak that can be seen at 538 cm^{-1} [48]. The E_1(LO) mode has also been designated to the peak at 585 cm^{-1}. The presence of impurities and structural defects on ZnO nanostructures explains the origin of this mode in the Raman spectra [43]. Additionally, interstitial zinc defects may be linked to the absorption band from approximately 80 to 190 cm^{-1} [47].

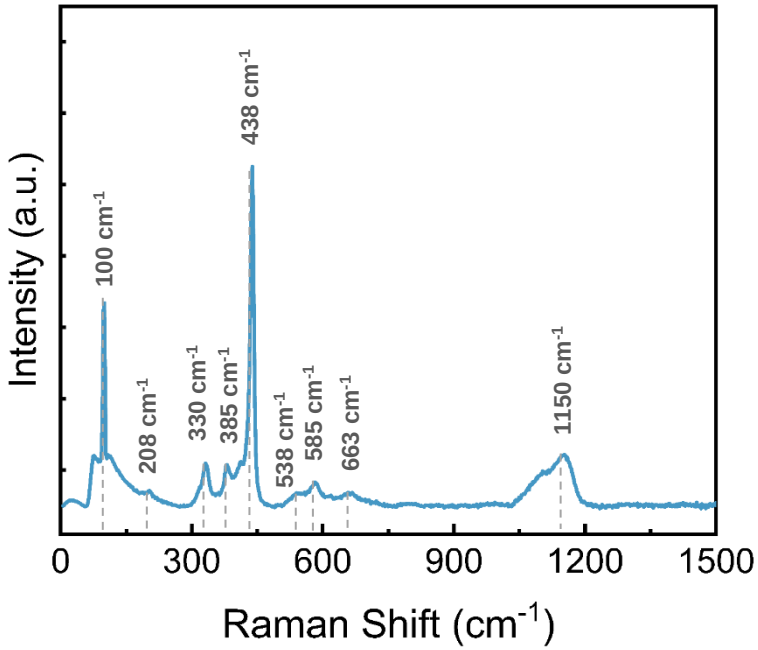

Figure 3.2: Room temperature Raman spectra of the as-prepared ZnO NWs.

Figure 3.3 (a) shows a SEM image of the synthesised ZnO nanostructures, where it is recognizable that the vast majority of the structures fit into the NW classification, morphologically similar to a wire, with a length greater than the diameter and with the width (or diameter) restricted to the nm scale. Figure 3.3 (b), which depicts the length/width ($\bar{l}$ / $\bar{d}$) distribution of NWs, confirms this notion by indicating an average $\bar{l}$ of (4.27 ± 2.31) µm and an average $\bar{d}$ of (490 ± 326) nm, both estimated from the Gauss fits represented in this

Figure 3.3, calculated from the measurement of 150 NWs. However, there is a significant variation in these two dimensions, as shown in Figures 3.3 (a) e (b). The length ranges from 1.4 to 11 µm, while the diameter ranges from 80 nm to 1.7 µm. Nevertheless, the length interval of 1 to 5 µm represents 75 % of the measured fibres, and 93 % of the diameters are between 100 and 900 nm. Since the vast majority of these structures have a width in the oroder of nanometer, these nanostructures fall within the definition of NWs.

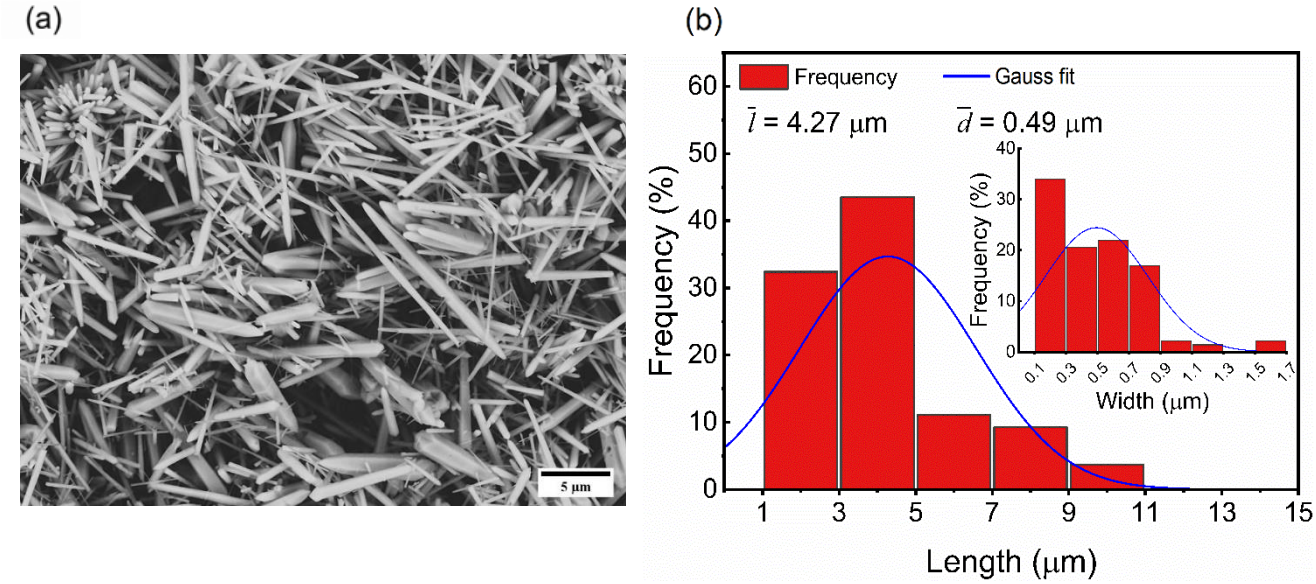

Figure 3.3: (a) SEM image of ZnO NWs. (b) Length/width distribution of the as-synthesized ZnO NWs.

The optical E_g was calculated using the Kubelka-Munk (K-M) method applied to the reflectance (R) data. Through this method, detailed in Annex C, the estimated E_g for ZnO NWs is 3.23 eV, which is in accordance with the literature [49,50]. This value of the optical E_g corresponds to a wavelength of 380 nm, which is in the UV-A range, demonstrating the well-known UV light detection capability of ZnO and, in particular, of these ZnO NWs.

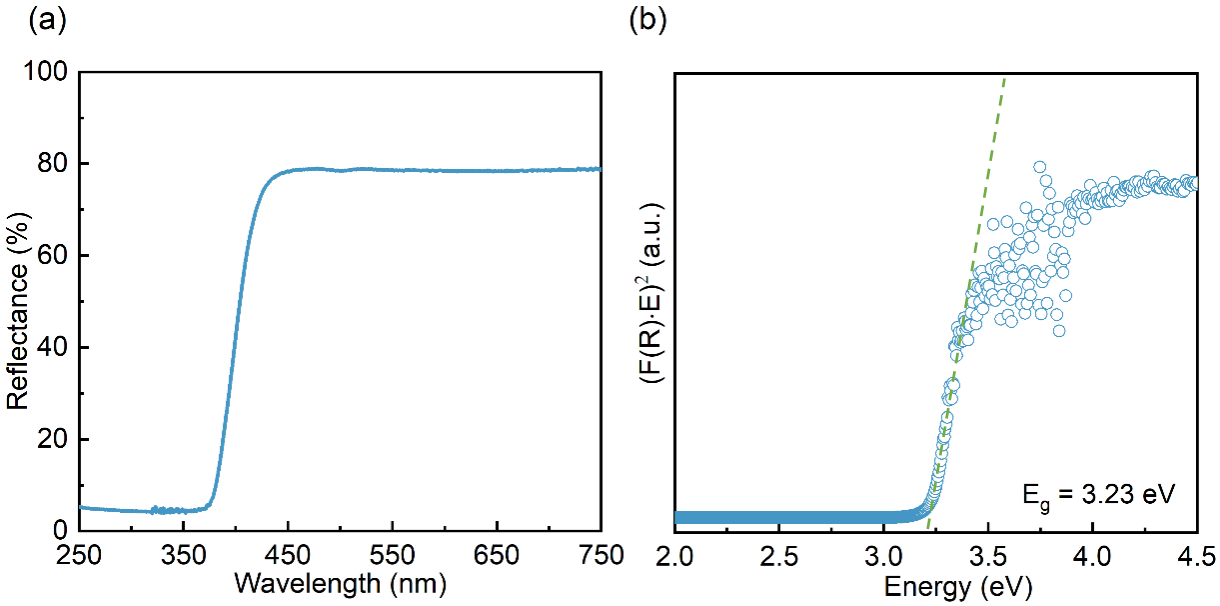

Figure 3.4: (a) Reflectance spectra of the ZnO NWs and (b) the modified K-M function (F(R)×E)2 versus the photon energy (E) in order to estimate the Eg by extracting the intersection of the extrapolation of the linear portion with zero in the Energy axis.

Figure 3.5 depicts the normalized PL spectra of ZnO NWs, revealing multiple emission bands in the blue (400-490 nm), green (500-550 nm), and yellow-orange (≈600 nm) regions of the spectra. From the PL spectra it is immediately apparent that the green and yellow-orange bands are more intense than the blue band. From the PL spectra, in the yellow-orange region it can be identified a main broad peak centered at approximately 590 nm. Several reports have shown the presence of this yellow-orange defect luminescence on ZnO nanostructures produced via solution-based methods and is typically related to excess of oxygen (e.g., oxygen interstitials) [51,52]. However, there is still no consensus on the precise cause of the defect-related visible PL of ZnO, green and yellow-orange emissions have been associated with structural defects and impurities which include: an oxygen vacancy (V_O), a zinc vacancy (V_{Zn}), an oxygen atom at the zinc position in the crystal lattice (O_{Zn}), a zinc atom at the oxygen position in the crystal lattice (Zn_O), interstitial oxygen (O_i), and interstitial zinc (Zn_i) [53,54]. The green emission peaks were detected on the PL spectra at 531 and 545 nm. As previously mentioned, this type of green emission is also related with different kinds of defects, however many research groups of have linked this emission to singly ionized oxygen vacancy ($V_O^{\bullet}$), which is supported by the fact that the intensity of green emission could be tuned by varying annealing temperature and atmosphere [55]. Based on the strong visible band that surpasses the blue and UV bands, we can conclude that this sample contains a high concentration of defects, which are most likely caused by the synthesis method and for the lack of a post-treatment.

The peaks found in the blue band were centered at 409, 426, 448, 463 and 488 nm, as shown in Figure 3.5. The transitions between the Zn_i and extended Zn_i levels and the valence band (V_B) have been identified as the sources of these blue emissions between 409 and 488 nm [47]. Although not visible in the graph, a peak at around 390 nm may be hidden by the ascending curvature that shapes the 409 and 425 peaks. Considering that ZnO has a free binding energy (E_x) of 60 meV, and the energy of the energy of the radiative recombination its equals to E_g-E_x, given the E_g value obtained of 3.23 eV, an emission around 3.17 eV (≈390 nm) should be expected. In another report, ZnO nanostructures with a very similar PL spectra, where the 390 nm peak was not visible in the graph was still identified by deconvoluting the spectra into several Gaussian components [47].

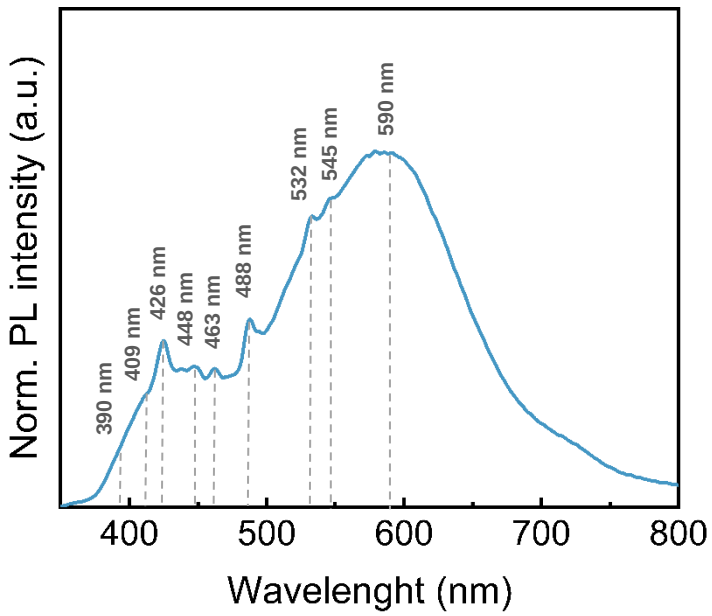

Figure 3.5: Photoluminescence spectra of the ZnO NWs sample measured with an excitation wavelength of 254 nm.

3.2 Synthesized ZTO NWs Characterization (structural, morphological, and optical)

The same techniques used to characterize the ZnO NWs were used to characterize the $ZnSnO_3$ NWs. The results presented here are a summary of the conclusions drawn from articles published by Rovisco *et al.*, the i3N/CENIMAT researcher who developed and extensively studied the hydrothermal synthesis of $ZnSnO_3$ NWs, which are used as the active layer of UV sensors in this work. The main goal is to demonstrate that the ZTO synthesis was successful and to better understand some properties that may shed light on some of the results that will be presented in the device's electrical characterization.

Due to the elemental composition of this multicomponent material, and as Rovisco *et al.* demonstrated, depending on several physical and chemical parameters, the synthesis can result in a mixture of different phases, beginning with the presence of both ZTO phases ($ZnSnO_3$ orthorhombic perovskite phase and Zn_2SnO_4 inverse spinel phase - ICDD card 00-024-1470), but also with residual tetragonal phase of SnO_2 (ICDD card 01-077-0452) and ZnO with hexagonal phase (ICDD card 00-036-1451). For this analysis, the ICDD card 00-028-1486 was used to identify the peaks that correspond to this specific $ZnSnO_3$ phase. It should be noted that even though this card was removed from the ICDD database, because of its resemblance to a mixture of Zn_2SnO_4 and SnO_2 phases, it is still mentioned in a number of literature reports [4,5].

The XRD diffractogram of the synthesized ZTO NWs is present in Figure 3.6. Since the nature of a multitude of different peaks that can be confused with the different phases already mentioned, an identification of the preeminent orth-$ZnSnO_3$ phase solely by the interpretation of XRD results is very complicated. However, an almost identical diffractogram to the one presented by Rovisco *et al.*, that showed the $ZnSnO_3$ orthorhombic perovskite phase prominence, it is present in Figure 3.6 [4,5].

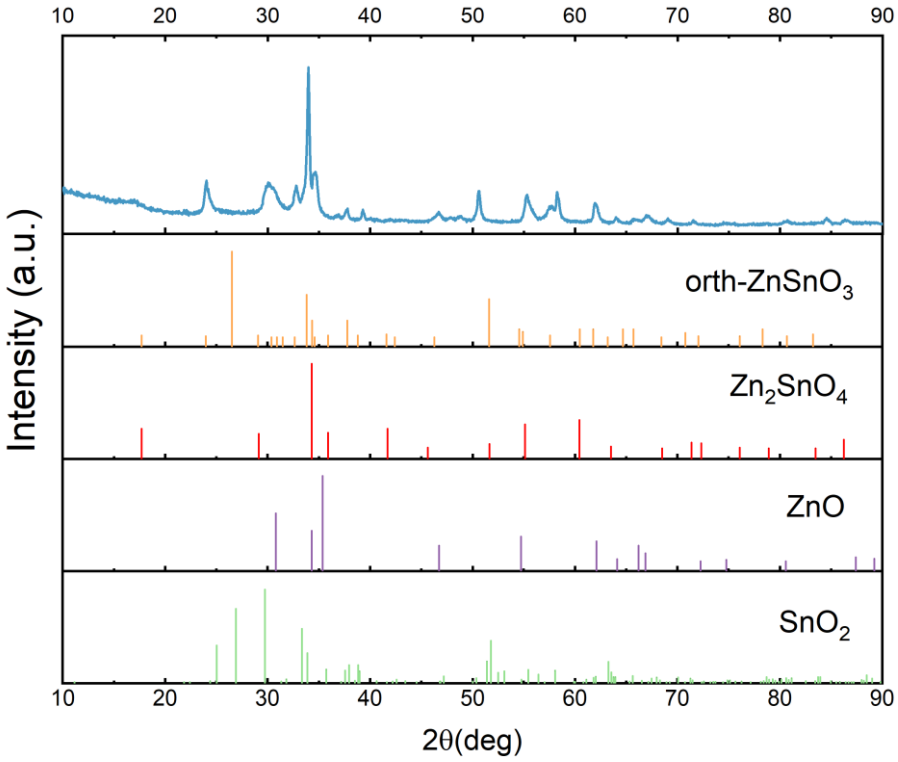

Figure 3.6: XRD diffractograms of the ZTO NWs synthesized via hydrothermal synthesis and representation of XRD peaks of ICDD cards of all the possible phases identified in the samples. The orth-ZnSnO3 card 00-028-1486 is represented to show the similarity with ZnS $ZnSnO_3$ nanowires data. This card was however removed from inorganic crystal structure data.

Through the interpretation of the results obtained by Raman spectroscopy, represented in Figure 3.7, and also with the SEM images of the synthesized nanostructures at Figure 3.8, it is possible to extract more conclusions that support the predominance of the perovskite $ZnSnO_3$ phase.

The two peaks that stand out in the Raman spectra are located at 538 and 676 cm^{-1}, corresponding to internal vibrations of the oxygen tetrahedron in Zn_2SnO_4 and to the characteristic Raman M-O bonds stretching vibration mode in the MO_6 octahedron of $ZnSnO_3$ and/or Zn_2SnO_4, respectively [4,5]. Although the peaks are characteristic of both ZTO phases, as Rovisco *et al*. found, when testing various synthesis conditions, that the $ZnSnO_3$ phase is predominant when the peak at 538 cm^{-1} (which corresponds only to the Zn_2SnO_4 phase) becomes less intense while the peak at 676 cm^{-1} becomes prominent. This being in accordance with the Raman spectra in Figure 3.7 where we can see a much more intense peak at 676 cm^{-1} [4,5]. Despite the presence of mixed phases, the results are consistent with the optimized synthesis previously reported by Rovisco *et al.*, indicating that predominantly orth-$ZnSnO_3$ phase was obtained.

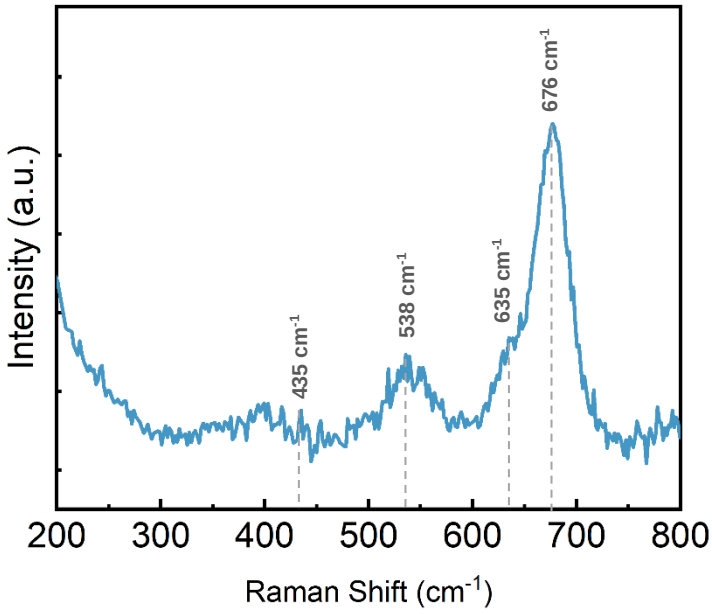

Figure 3.7: Room temperature Raman spectra of the as-prepared ZTO NWs.

This is also corroborated by the SEM images, as the vast majority of the nanostructures obtained were NWs, with only a few nanoparticles detected that are shown in Figure 3.8.

The researcher's studies have revealed the formation of additional nanostructures that indicate the presence of other phases that have already been mentioned, including Zn_2SnO_4 (in the form of NWs, octahedrons, nanoparticles and nanocrystals), ZnO (as columnar nanoplatelets), and SnO_2 (in the form of nanoparticles) [4,5]. In SEM images, a notable majority of NWs and only a few nanoparticles can be seen, in Figure 3.8. The nanoparticles may be related to Zn_2SnO_4 inverse spinel phase and to tetragonal phase of SnO_2 since these phases exhibits a few peaks in common with the sample's XRD data. Moreover, a small, nearly indecisive Raman peak that rises at 635 cm^{-1} in the Raman spectra can be identified. This peak is associated with the expansion and contraction of the Sn−O bond peak and supports the previous statement [4].

In any case, the appearance in the SEM images of few nanoparticles serve to reinforce the assumption that, despite the possibility of some residual Zn_2SnO_4 and SnO_2, orth-$ZnSnO_3$ NWs are primarily obtained.

The existence of ZnO in the form of hexagonal microtubules was also reported in the published papers referring to this synthesis, when tested under the conditions that were used here [4]. This evidence was supported by the identification of two Raman peaks characteristic of this material [4,5]. While one of the peaks,

located at 435 cm^{-1}, can be remotely identified, there appears to be no signal from the second peak, which is located at 574 cm^{-1}. Moreover, in the SEM images, no sign of this structure was found.

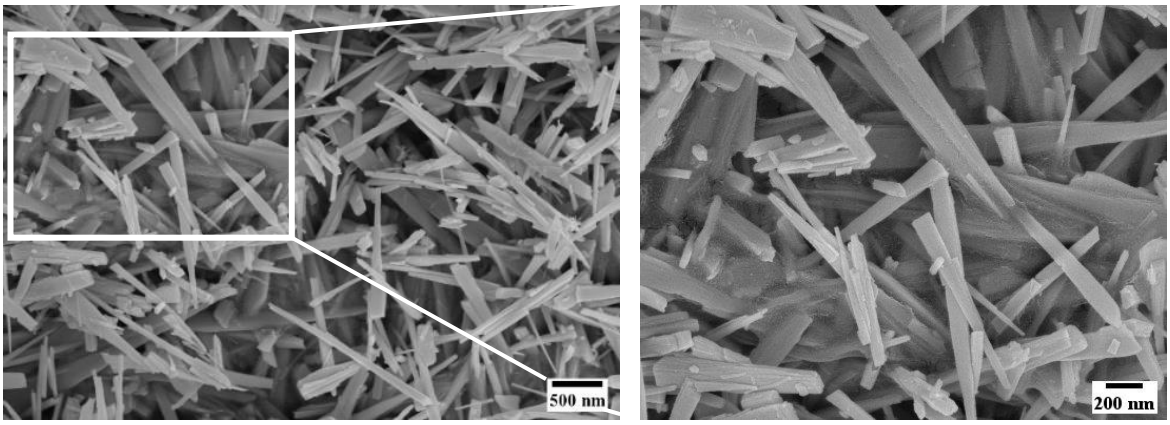

Figure 3.8: SEM images of the nanostructures obtained via hydrothermal synthesis. The image on right, which is an amplification of the region demarcated by a rectangle in the left image, allow for the identification of few nanoparticles, despite $ZnSnO_3$ NWs being the most prevalent structure observed.

The length/width ($\bar{l}$ / $\bar{d}$) distribution of the NWs is shown in Figure 3.9 (a), which averaged is $\bar{l}$ / $\bar{d}$ = (796 ± 515) nm / (68 ± 40 nm), estimated from Gauss fits represented in the Figure 3.9, calculated from the measurement of 150 NWs. The NWs have a wide range of lengths, as shown in Figures 3.8 and 3.9. The shortest measured length was 118 nm, and the longest was 2.74 µm. However, the large percentage of the measured NWs, approximately 40 %, fall between 418 and 718 nm. Regarding the NWs' diameter, it is comprised in narrower range of sizes. The smallest diameter measured was 14 nm, and the largest was 214 nm. As shown in Figure 3.9, 70 % of the NWs have a diameter lower than 90 nm and 30 % have a diameter ranging from 34.5 to 68.5 nm. Finally, it is noted that the NWs' $\bar{l}$ and $\bar{d}$ are very close to those reported by *Rovisco et al.*, thus reinforcing that the synthesis produced mostly orth-$ZnSnO_3$.

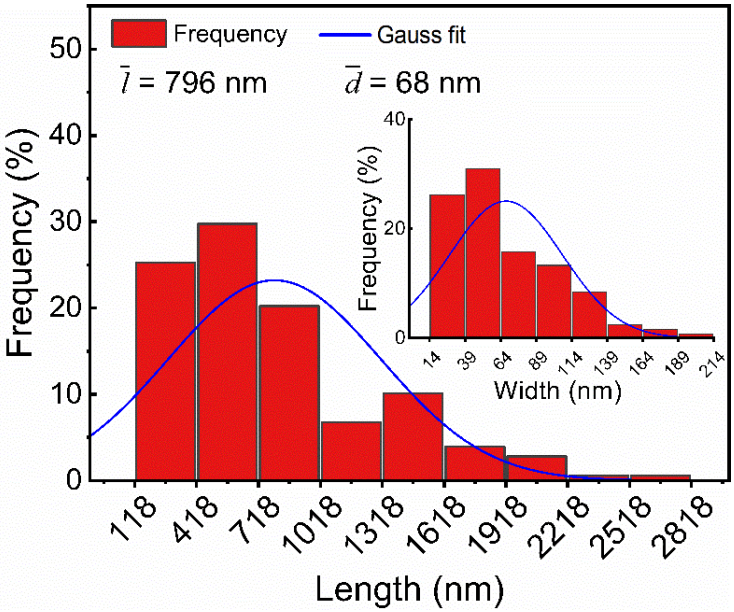

Figure 3.9: Length/width distribution of the as-synthesized ZTO NWs.

The K-M method was applied to the reflectance data presented in Figure 3.10 (a), thus giving rise to Figure 3.10 (b) from which the optical E_g of the ZTO NWs was estimated to be 3.89 eV. This value of the optical E_g corresponds to a wavelength of 318 nm, which is in the UV-B range, demonstrating the potentiality of these ZTO NWs to detect selectively a more energetic UV light. However, since the E_g of these NWs is greater than the energy corresponding to the λ of the UV LED (360 nm ≈ 3.44 eV) used in the electrical characterization, the I_{ph} produced ought to be lower because the direct photoconductive effect between the V_B and C_B will not occur.It should be noted that this E_g value is within what has been reported in the literature for $ZnSnO_3$ nanostructures (3.3-3.9 eV) [56,57].

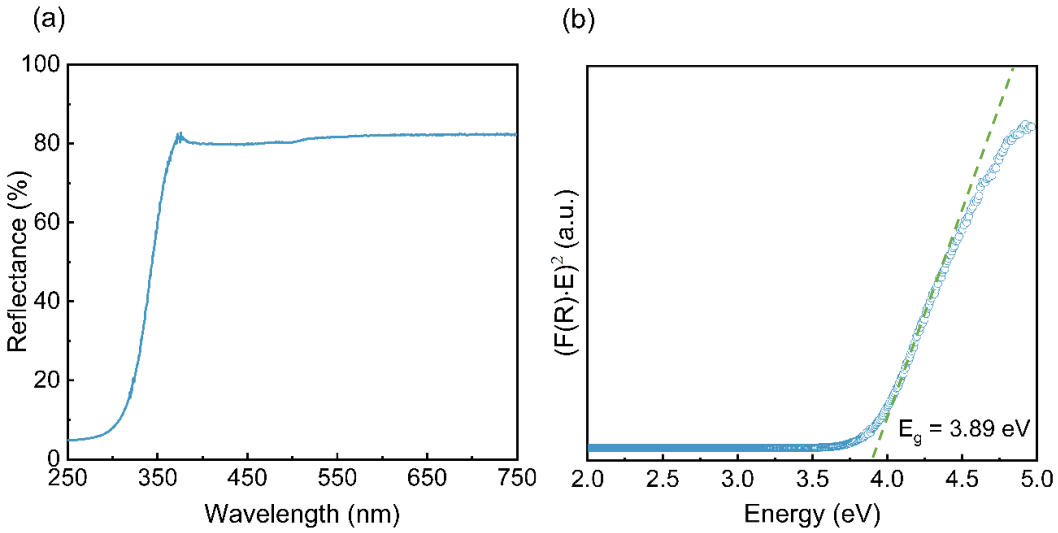

Figure 3.10: (a) Reflectance spectra of the ZnO NWs and (b) the modified K-M function (F(R)×E)2 versus the photon energy (E) in order to estimate the Eg by extracting the intersection of the extrapolation of the linear portion with zero in the Energy axis.

The emission peaks observed in the PL spectrum presented in Figure 3.11, are distributed by the visible region, where are demarcated the blue bands (peaks centered at 425, 446, 462 and 488 nm), the green band (peak centered at 530 nm) and the green-yellow region (broad peaks centered at 573 and 599 nm). It is also noted that the existence of the most intense peak is located in the UV region, at 372 nm.

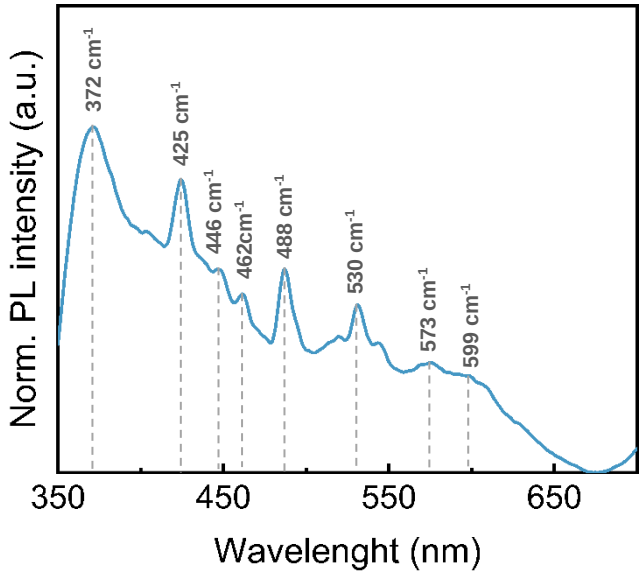

Figure 3.11: Photoluminescence spectra of the ZnO NWs sample measured with an excitation wavelength of 254 nm.

The UV emission peak, centered at 372 nm, is a feature linked to the band-to-band emissions for the E_g of $ZnSnO_3$ (3.3-3.9 eV) [56], agreeing with the reflectance results. The formation of 425 and 488 nm peaks is connected with V_O's and/or O_i's, which are major defects in this type of material, since emissions in this region are common for ZTO nanostructures [28,57]. The existence of V_O's is also attributed to the 462 nm emission peak [58]. The emission at 446 nm is associated with the transition from shallow donors (related to V_O's) to the V_B [56,59]. It should be noted that the UV and blue band emissions are the most intense and stand out from the other emissions, as is illustrated in Figure 3.11.

The green emission (529 nm) is generally referred as deep-level emission, caused by radiative transitions between shallow donors and deep acceptors (V_{Zn} and Sn vacancies) [57]. Lastly, the emission in the yellow-green region (573 and 599 nm) is attributed to the recombination of V_O with holes [60].

Although the existence of some structural defects is evidenced, especially V_O's, the PL spectra of the as-synthesized ZTO not only helps to confirm that the synthesis resulted mostly in orth-$ZnSnO_3$ but also denotes the potentiality of these NWs in their application in UV sensors.

3.3 Electrical Characterization of ZnO-based UV sensors:

As explained previously, the UV sensors were tested by applying 1, 5 and 10V to the sensor's contacts, thus studying the effect of the applied voltage. Simultaneously, by fixing the applied voltage, a study of the finger spacing effect was conducted, with finger spacings of 10, 30, and 50µm. To summarize, under different applied voltages, all different finger spacings of the interdigitated electrode configuration were tested. The objective was to understand how the sensor behaved by tracking how its characteristic parameters (described in Chapter 1) evolved when subjected to different conditions to better understand the influence of these conditions on the UV response of this devices.

Figures 3.12 (a) and (b) show the current-voltage (I-V) characteristics with linear and semi-log scales, respectively.

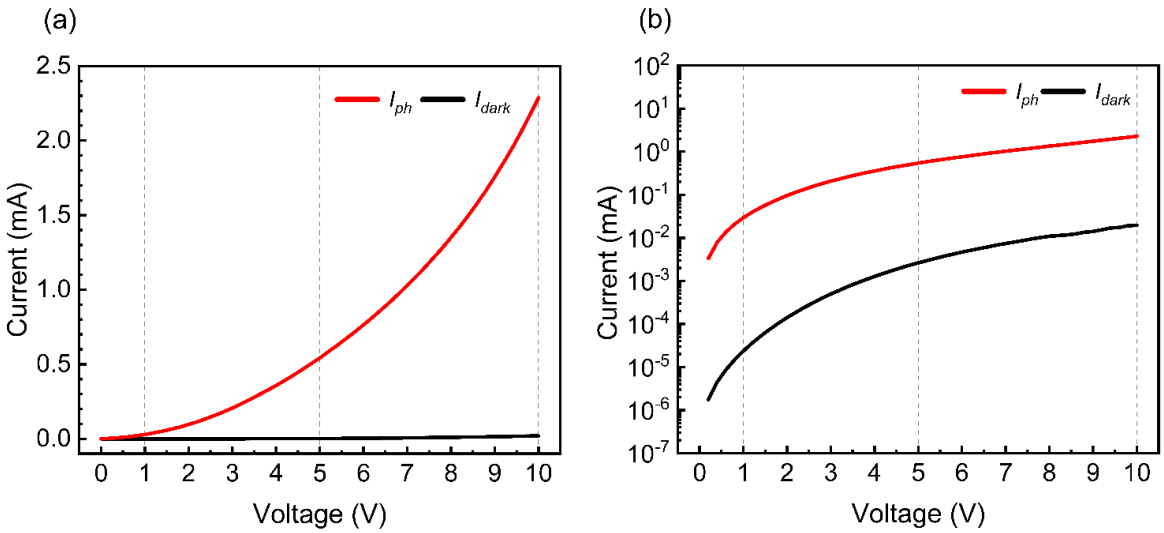

Figure 3.12: (a, b) I–V characteristics in a linear and semi logarithmic scale, respectively (PUV = 2.6 mW, λ = 365nm).

The different operating regions tested are demarcated on Figure 3.12 (a) and (b) in grey dashed lines, at the corresponding voltages of 1, 5 and 10 V. Figure 3.12 (b) shows a significant rise in the I_{ph}, which increases by 2 to 3 orders of magnitude compared to the I_{dark} and, naturally, presents itself as a desirable feature for the detection of UV radiation. The ratio between the currents is slightly greater than 3 orders of magnitude for lower voltages, as already noted, but it can be seen that as voltage increases, this difference decreases until the lowest ratio of 2 orders is eventually obtained when 10V are applied.

3.3.1 Time-dependent photoresponse: Finger spacing influence

The time-dependent photoresponse of fabricated ZnO-based UV sensors, for all finger spacings (10, 30 and 50µm) with a fixed applied voltage of 1 V, was measured by periodically switching a 365 nm UV light with a P_{UV} of 2.6 mW, as shown in Figure 3.13. For the sensors with 30 µm finger spacing electrodes three replicas were performed and for those with 10 and 50 µm only two, with the purpose of investigating the reproducibility of the devices.

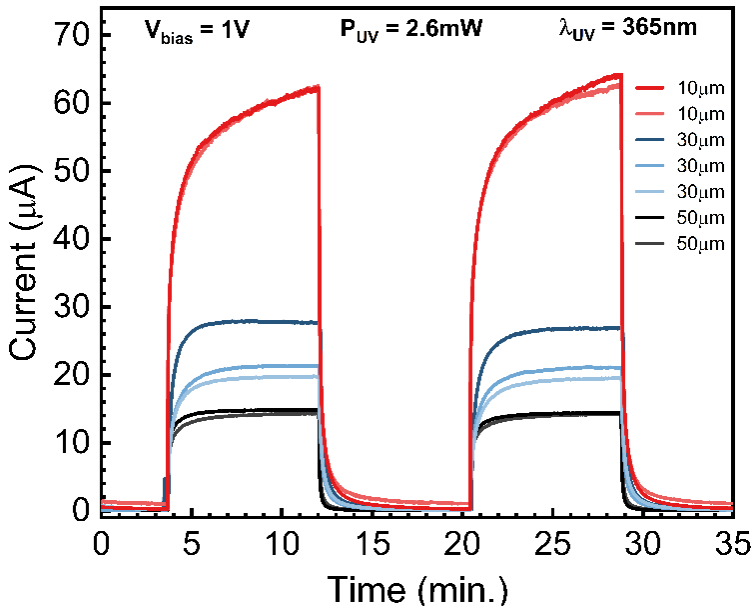

Figure 3.13: ZnO-based UV sensor time-dependent photoresponse of ZnO-based UV sensors at a constant bias voltage of 1 V (P_{UV} = 2.6 mW, λ = 365nm). Lines depicting the performance of the 10 µm sensors are in red tones, 30 µm sensors in blue tones and 50 µm sensors in black tones.

The parameters characterizing the UV response of all the sensors tested with 1 V of applied voltage, were extracted from the time-dependent photoresponse in Figure 3.13 and are presented in Table 3.1 as a function of their finger spacing.

Table 3.1: ZnO-based UV sensor parameters obtained as a function of finger spacing of 50, 30 and 10 µm at a fixed applied voltage of 1V, with two samples for the 50 and 10 µm spacings and three samples for the 30 µm.

		1 V						
Finger Spacing (µm)	***Sample***	t_{rise} **(s)**	t_{fall} **(s)**	I_{ph} **(µA)**	I_{dark} **(µA)**	I_{ph}/I_{dark} **(u.l)**	ΔI **(µA)**	R_{UV} **(mA/W)**
50	***S1***	70	20	14.3	0.04	357	14.3	5.5
	S2	43	12	14.5	0.03	483	14.4	5.6
30	***S1***	98	49	19.7	0.09	218	19.6	7.5
	S2	94	34	21.3	0.11	193	21.2	8.3
	S3	89	41	27.7	0.16	173	27.5	11.1
10	***S1***	175	30	62.2	0.98	63	61.2	23.5
	S2	162	32	62.1	0.25	248	61.8	23.7

From Figure 3.13 and Table 3.1, it is possible to state that the smaller the finger spacing the higher the I_{ph} produced by the sensors. Not only is the electric field to which free electrons are subjected higher, favoring charge separation, but also the path that they need to travel before being collected by the electrodes is shorter

(thus decreasing the probability of recombination). The same logic applies to the I_{dark}, which is larger in devices with narrower spacing, which in turn results in a lower I_{ph}/I_{dark} the smaller the spacing, as can be seen in the Table 3.1. Although the aforementioned increase in I_{ph} is accompanied by an increase in I_{dark}, ΔI and R_{UV} also increase with the decrease in finger spacing.

Regarding the response times, it is observed that, for smaller spacings, the t_{rise} and t_{fall} increase considerably. However, the t_{fall} of the 10 µm sensor is lower than that of the 30 µm sensor, contradicting the trend of an increase in t_{fall} with decreasing spacing. This can be justified by the fact that the 10 µm sensors do not stabilize their I_{ph} after 500 s of UV exposure, as presented in Figure 3.13. This indicates an aggravation of the persistent increase in conductivity (concept explained further) when the finger space is decreased. It should be added that even the shortest t_{rise} and t_{fall} recorded for the 50 µm spacings are still quite high (between 40 and 70 s).

As previously mentioned in the Introduction Chapter, the UV sensing mechanism of metal oxide nanostructures is predominantly governed by the adsorption and desorption of oxygen molecules on the nanostructures' surface. The presented results are consistent with this model, with the initial abrupt increase in I_{ph} being observed in all the sensors tested - a representative example is the case of S2 with 50 µm spacing, in which the I_{ph} current goes from 0.036 µA to 4.7 µA in just 1 s.

Furthermore, the adsorption-desorption phenomenon is believed to influence the UV response of these nanostructures by extending their photocarrier life-time. The gradual and prolonged nature of these processes leads to a persistent increase in conductivity [55]. In fact, as shown in Figure 3.13, when the UV light is on, the electrical conductivity, after the abrupt rise, increases gradually over time, resulting in prolonged t_{rise}. Naturally, this effect is more evident with the decrease of the finger spacing (when the electric field is stronger), with 10 µm spacing being the most obvious case.

Ultimately, it is possible to link the slow UV response of these sensors to the structure of the synthesized ZnO NWs, which, as seen through PL analysis, is marked by a number of defects, with green and yellow-orange emissions resulting in a prominent broad peak. Additionally, Tzeng *et al.* demonstrated how the suppression of this broad peak by a hydrothermal treatment can decrease V_O and, in turn, significantly shorten the t_{rise} and t_{fall} of the corresponding ZnO-based sensors [55].

Furthermore, the prolonged t_{fall} may be due to the fact that when the UV light is turned off, although many electrons and holes recombine quickly, many others are left without recombination. Since oxygen readsorption is responsible for capturing these unpaired electrons, and this is a slow and gradual process, the t_{fall} become long [39].

To investigate defects' impact on the sensors photoresponse, UV sensors with the same interdigital configuration were fabricated but using as the active layer a ZnO thin film deposited via sputtering, with the results presented in Annex D. Despite not being nanostructures, the theoretical thin film's low-defect structure led to fast response times (t_{fall} = 0.79s and t_{rise} = 19 s) and higher I_{ph}/I_{dark} (> 10^3) .

Regarding the devices' ability to be replicated, although Figure 3.13 appears to demonstrate some reproducibility between samples, Table 3.1 reveals that the parameters, particularly the response times exhibit significant variability. This variation may be caused by the drop-casting method, which, despite being done in a controlled manner, always end up dispersing the NW's randomly, as shown in in Annex B, which shows the dispersion of NWs on top of the finger electrodes. It should also be noted that, the current-related parameters (I_{ph}, ΔI, and R_{UV}) exhibit some degree of reproducibility, with the exception of the I_{ph}/I_{dark}, which ends up varying significantly due to the variation that also occurs in the I_{dark}.

It should be highlighted that the finger spacing decrease had the same effect on the sensors when 5 and 10 V were applied and displayed only a different nuance when compared to the 1 V tests. The results of the tests conducted on the sensors with 50 and 30 µm spacing when exposed to 5 and 10 V voltage are presented in Annex E. Once more, at higher voltages it is still observed that higher I_{ph} and I_{dark} values are correlated with

narrower finger spacing, which again leads to lower I_{ph}/I_{dark} but also higher ΔI and R_{UV}. However, the t_{rise} does not follow the same pattern as it did at 1 V. The t_{rise} is shorter for the sensors with a narrower spacing for both 5 and 10 V, as indicated in Table E.1 in Annex E. In turn, the t_{fall} is longer for the narrower sensor tested. It should be noted that both 50 and 30 µm sensors did not stabilize their currents after the period of UV light exposure for applied voltages of 5 and 10V which allow us to conclude that for higher applied voltages the persistent increase in conductivity is aggravated.

3.3.2 UV sensor response to different voltages

The time-dependent photoresponse of 50 µm sensors for applied voltages of 1, 5 and 10 V is depicted in Figure 3.14 (a) and (b), in linear and semi-log scales, respectively. The same analysis was carried out for 30 µm sensors, the results of which are presented in the Annex F, with the same line of conclusions drawn to this different spacing. First off, larger I_{ph} and I_{dark} are achieved for higher applied voltages, as we can deduce from Figure 3.14 (a) and (b), leading to higher ΔI and R_{UV} but once again at the cost of longer response times and lower I_{ph}/I_{dark}. Figure 3.14 (b) clearly shows this decrease in I_{ph}/I_{dark} with increasing applied voltage. At 1 V more than two orders of magnitude separate I_{dark} from I_{ph}, at 5 V slightly less than two orders, and barely an order at 10 V.

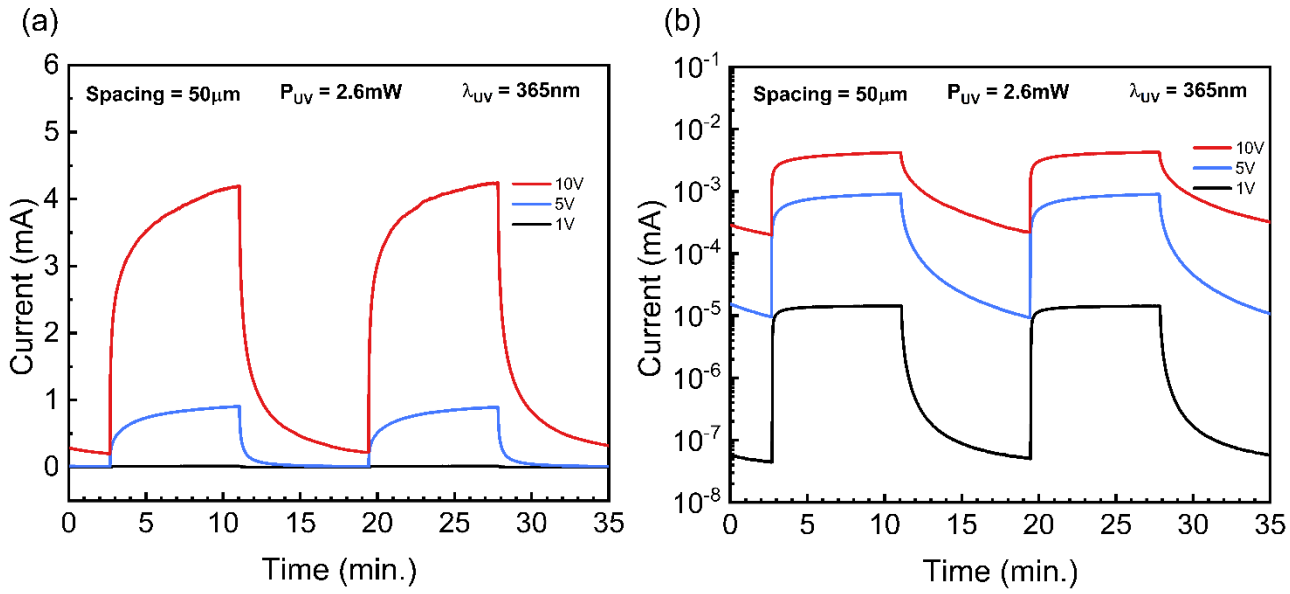

Figure 3.14: (a, b) ZnO-based UV sensors time-dependent photoresponse at different bias voltages of 1, 5 and 10 V in a linear and semi-logarithmic scale, respectively.

Table 3.2 presents a comparison of the parameters obtained from figure 3.14. It is important to note that, as shown in Table 3.2, when the applied voltage is increased from 1 to 5 V, the increase in I_{ph} happens by shifting from the µA to the mA scale, reflecting a considerable increase. The same scale transition is shown in ΔI, and a change from mA/W to A/W is seen with regard to R_{UV}. Once more, we see the impact of the electric field that produces a I_{dark} at a voltage of 5 V approximately equal to the I_{ph} achieved at 1 V, as seen in Figure 3.14 (b).

Table 3.2: ZnO-based UV sensor parameters obtained as a function of an applied voltage of 1, 5 and 10 V for a finger spacing of 50 µm.

		Finger Spacing = 50 µm						
Applied voltage bias (V)	***Sample***	t_{rise} **(s)**	t_{fall} **(s)**	I_{ph} **(mA)**	I_{dark} **(µA)**	I_{ph}/I_{dark} **(n.l)**	ΔI **(mA)**	R_{UV} **(A/W)**
1	***S1***	43	12	$14 \cdot 10^{-3}$	0.03	483	$14 \cdot 10^{-3}$	$5.6 \cdot 10^{-3}$
5	***S1***	228	62	0.91	9.2	96	0.90	0.34
10	***S1***	172	156	4.24	220	19	4.02	1.54

To summarize, the impact of rising the applied voltage and decreasing the finger spacing is very similar. In essence, both end up increasing the electric field, resulting in higher currents (I_{ph} and I_{dark}), higher ΔI and R_{UV} and conversely in lower I_{ph}/I_{dark} and longer response times. Additionally, it can be seen that by increasing the applied voltage to 5 V, the decrease in spacing appears to result in a reduction in the t_{rise}, which is the opposite of what was seen at 1 V – one possible explanation being that for higher voltages the stabilization of currents becomes more difficult. Nonetheless, increasing the voltage always causes the t_{rise} and t_{fall} to be longer. It should be added that in order to draw more representative conclusions about the applied voltage effect more sensors would have to be tested.

3.3.3 UV illumination power influence

The influence of the incident UV illumination Power (P_{UV}) on the sensors photoresponse was also studied in order to characterize the operation of the sensors more deeply. Having selected seven P_{UV} values: {0.05, 0.70, 1.70, 2.60, 3.50, 4.70 mW}, tests were performed to extract the S_{UV} parameter, as discussed in the Introduction chapter, simultaneously investigating how the R_{UV} evolved with different P_{UV}.

Figure 3.15 (a) displays the time-dependent photoresponse of ZnO UV sensors with 30 µm finger spacing at a constant applied voltage of 1 V. The P_{UV} varies every 200 seconds for the predetermined values, beginning with the light off and increasing to a maximum P_{UV} of 4.70 mW before decreasing for the same values and at the same step. The same type of graph is shown in the Annex G with respect to the 50 µm sensors. Figure 3.15 (b) displays the ΔI calculated from Figure 3.15 (a) as a function of the P_{UV}, allowing us to evaluate the S_{UV}. Due to the nearly linear relationship between the variation of ΔI with P_{UV}, except for the first data point, linear fittings were applied to the remaining data points in the graph. This approach enabled the extraction of the S_{UV} through the slope of the corresponding linear fittings. In the same Figure 3.15 (b), the variation of the R_{UV} with respect to the P_{UV} is also presented.

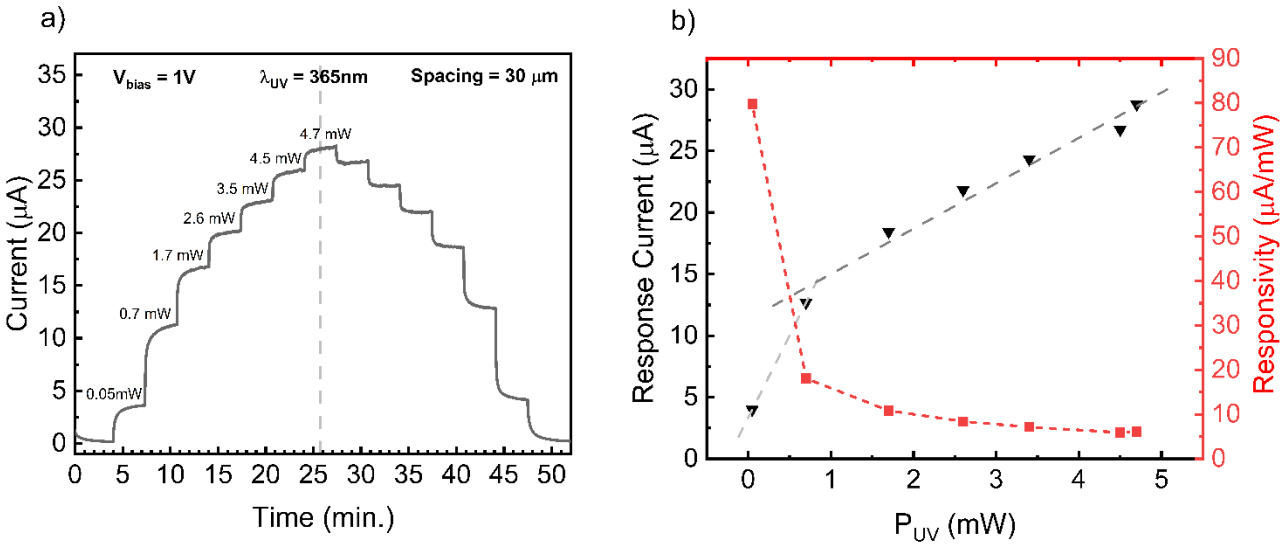

Figure 3.15: (a) Time-dependent photoresponse to a constant bias voltage of 1V, increasing the P_{UV} progressively every 200 s (to the values marked on top of each current plateau) - left half of the graph; and then decreasing the P_{UV} to the same values at the same rate until the UV light is turned off - right half of the graph. (b) ΔI calculated from (a) as a function of the previous mentioned values of P_{UV}, marked by black points with the two grey dashed lines corresponding to two different S_{UV} regimes. In the same graph, marked by red square points with a dash red line connecting them, the R_{UV} calculated from (a) is plotted as a function of P_{UV}.

It should be noted that the ΔI and R_{UV} values shown in Figure 3.15 (b) were calculated using the maximum I_{ph} values obtained for each P_{UV} value during the phase of P_{UV} declining (shown in the right half of Figure 3.15 (a)). This information is noteworthy because hysteresis is observed between the maximum I_{ph} values recorded when P_{UV} values are increasing and when P_{UV} values are decreasing. The resulting graphs of ΔI (calculated from both halves of the graph in Figure 3.15 (a)) as a function of P_{UV}, for 30 and 50 µm sensors, are depicted in Figure 3.16 and show more clearly how hysteresis is present. The maximum difference in ΔI points between rising and falling P_{UV}´s is 0.78 µA for 50 µm sensors and 1.83 µA for 30 µm sensors, corresponding to 4.6 % and 7.1 % of the sensor span, respectively. The verified hysteresis may be a result of insufficient time at the P_{UV} increasing stage for I_{ph} to stabilize at its maximum value.

Concerning the ΔI of the sensors, represented with black triangle points at Figure 3.15 (b), it is straightforward to affirm that this this parameter increases with P_{UV}. Looking only at the first two points in

Figure 3.15 (b), the increase in ΔI with P_{UV} translates into a shift from 3.99 µA for 0.05 mW to 12.67 µA for 0.7 mW. Although they do not represent the greatest increase in P_{UV} values, these first two points show the greatest increase in ΔI between two adjacent points, distinguishing them from the remaining points that show a more gradual increase. The two grey dashed lines in Figure 3.15 (b), which represent a straight line connecting the first two points and a linear fitting between the second and the other points, demonstrate these two types of behavior. The straight dashed line connecting the first two points has a much steeper slope than the linear fitting made between the remaining points, which translates into a much higher S_{UV} for lower P_{UV}´s (the S_{UV} between the first two points is equal to 13.35 µA·mW^{-1}, while the S_{UV} between the second and remaining points is (3.68 ± 0.31) µA·mW^{-1}. Despite the fact that this behavior is only described by two points (more points between these two P_{UV} values should be tested to draw more consistent conclusions), these two different types of UV response depending on the P_{UV} can be divided into two regimes: one for lower P_{UV} - between 0.05 and 0.7 mW, where the ΔI grows abruptly and consequently the S_{UV} is higher, and a second one – between 0.7 and 4.7 mW, where the ΔI continues to increase with P_{UV} but at a slower rate.

When the S_{UV} of 30 and 50 µm sensors extracted from the curves depicted in Figure 3.16 is compared, it is observed that the narrower finger spacing produced higher S_{UV} for both P_{UV} regimes. The 30 µm sensor generated more 4 µA·mW^{-1} in the lower P_{UV} regime and more 1.25 µA·mW^{-1} in the higher P_{UV} regime, both in the fall and rise of P_{UV}.

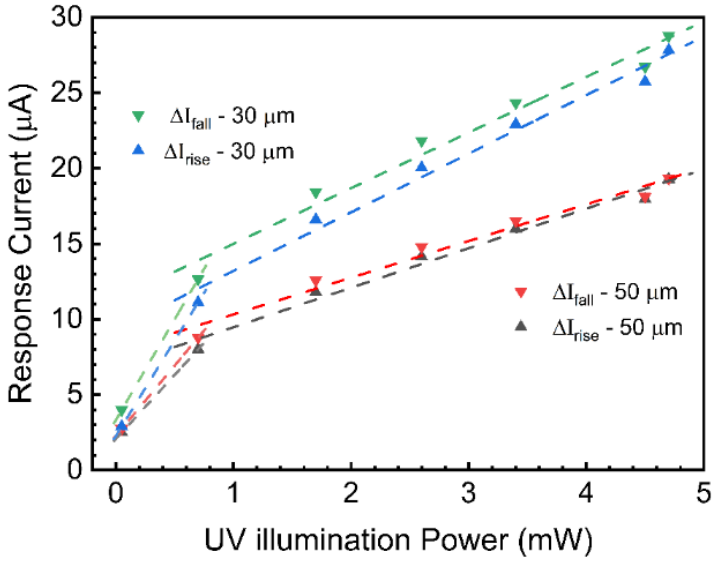

Figure 3.16: ΔI as a function of P_{UV}, calculated from when P_{UV} is rising (ΔI_{rise}) and when it is falling (ΔI_{rise}), with the corresponding linear fittings marked by the dashed lines, that reflect the two different S_{UV} regimes, for the sensors with 50 and 30 µm of finger spacing.

Furthermore, in both regimes described, the ΔI of the sensor in Figure 3.16 exhibits an approximate linear ascending trend. This suggests that the carrier density and the intensity of UV light are positively correlated, as increased P_{UV} results in more incident photons, more carriers being produced, and ultimately in higher ΔI [15,38]. In light of this, increasing the number of electron-hole pairs excited by powerful UV irradiation can significantly increase the conductivity of the UV sensor. On the other hand, the produced UV sensors can respond to much weaker UV light, as evidenced by the sensor's higher sensitivity for lower P_{UV}, making these sensors also suitable for the detection of low levels of UV light.

Regarding the R_{UV} represented in Figure 3.15 (b) in red, it is possible to verify that it decreases as P_{UV} increases. This is to be expected given that P_{UV} increases from 0.05 to 4.70 mW while the ΔI remains in the same range of the µA scale.

3.4 Electrical Characterization of ZTO-based UV sensors

This sub-chapter presents the electrical characterization of ZTO-based UV sensors. As was already mentioned, it is the first time that $ZnSnO_3$ NWs produced by solution methods have been employed as the active material of UV sensors. The ZTO sensors were characterized using the same methodology that were used to characterize the ZnO-based UV sensors.

3.4.1 Time-dependent photoresponse: Finger spacing influence for 1V

Figure 3.17 (a) shows the time-dependent photoresponse of the 50, 30 and 10 µm ZTO sensors with 1 V of applied voltage. For these tests the duration of the On/Off cycles was decreased to 30 s On and 30 s Off because the response to UV radiation for all 3 spacings proved to be weaker (the produced I_{ph} remained in the pA range) and not very stable. This modification was made only for the 1 V tests because it was counterproductive to try to stabilize the I_{ph} for 500 seconds On and 500 seconds Off at this voltage given the low signal.

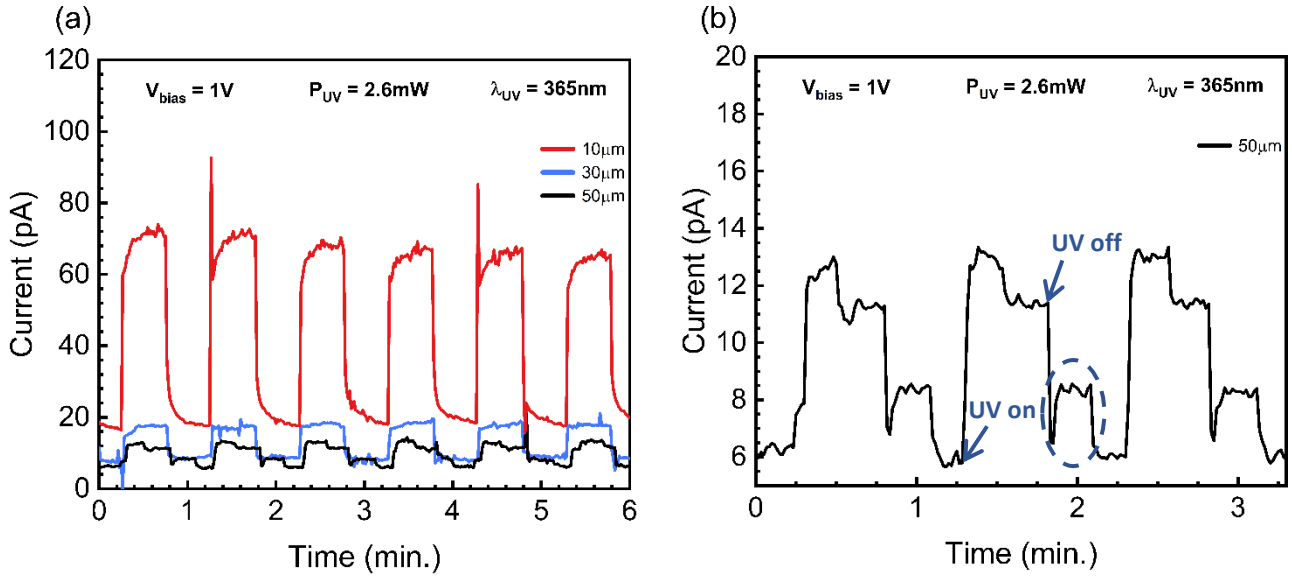

Figure 3.17: (a) ZTO-based UV sensor time-dependent photoresponse at a constant bias voltage of 1 V (P_{UV} = 2.6 mW, λ = 365nm). Lines depicting the performance of the 10 µm sensors are in red, 30 µm sensors in blue and 50 µm sensors in black. (b) Focus on three cycles of 50 µm sensor, highlighting the phenomenon of unexpected increase of I_{dark} (when the UV light is off).

The maximum I_{ph} generated for the 50 µm sensors was 13 pA, and both in the dark and during the UV exposure period, the values exhibited significant oscillation. Figure 3.17 (b), which shows three cycles of the 50 µm sensors, reveals that the generated I_{ph} initially reaches a maximum and then drops after a short period of time, oscillating in a lower range of values (thus going from values around 13 pA to values close to 11 pA). Another strange occurrence happens when the UV light is switched off. As illustrated in one of the cycles, in Figure 3.17 (b), after the LED is turned off, the current drops abruptly and suddenly rise again. As a result, it reaches a third plateau, around 8 pA that lasts approximately 10 s, and then drops again before the LED is turned on. Although quite unstable and with a very low signal, the ZTO sensors with 50 µm of finger spacing and only 1 V of applied voltage already demonstrate a response to UV radiation. Considering the different

duration of the cycles and their instability we denote that the 50 μm sensor presented a τ_{fall} of 10 s, a τ_{rise} of 1.3 s, an I_{ph}/I_{dark} of 2.4 and a R_{UV} of 3 nA·W^{-1}.

Proceeding to the 30 μm sensors, it is ascertained a slight increase in I_{ph} and I_{dark}, with the I_{ph}/I_{dark} remaining the same as for the 50 μm sensors. It should be noted that the previously described current oscillations are no longer identified with this decrease in finger spacing. The recorded τ_{fall} is lower, becoming 1 s, due to the absence of the unexpected increase in current which was previously observed. On the other hand, the τ_{rise} slightly increases because the current is stable and uninterrupted throughout the cycle, becoming 4.7 s. In relation to the R_{UV} there is a slight increase, registering now 4 nA·W^{-1}.

The 10 μm sensors exhibit the most significant differences. The sensor's I_{ph} increases to 72 pA, and I_{dark} rises to 17 pA (higher than the I_{ph} of the 50 and the 30 μm sensors). Additionally, it should be noted that for this spacing, 30 s in dark does not appear to be sufficient for the I_{dark} to stabilize and reach its minimum value. The resulting I_{ph}/I_{dark} is also larger and becomes almost twice that of the previous two sensors discussed, with I_{ph}/I_{dark} reaching 4.2. Regarding R_{UV}, a more pronounce increase is observed, registering 21 nA·W^{-1}.

Moreover, several sensors have demonstrated the ability to maintain very similar behavior, preserving the same characteristics and parameters within a narrow range of values, cycle after cycle.

3.4.2 Time-dependent photoresponse: Finger spacing influence for 10V

When 5 V and later 10 V are applied to the sensor terminals, the previously observed instability disappears - unlike ZnO NWs, ZTO NWs still require a higher voltage to show a stable UV response. As shown in Annex H, when a voltage of 5 V is applied to the ZTO sensors, the sensors are already closer to an ideal behavior, where the I_{ph} and I_{dark} reach a stable state after some time and do not exhibit current oscillations. Thereby, the ON/OFF cycles of 500 s of UV exposure and 500 s in the dark are restored.

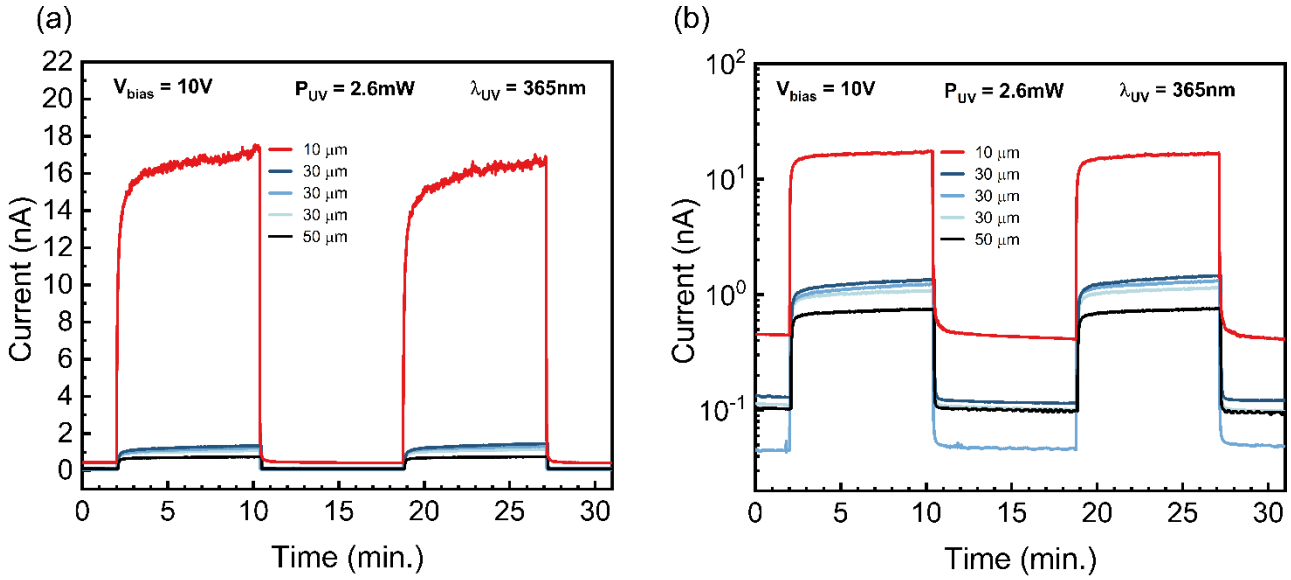

Figure 3.18: (a, b) ZTO-based UV sensor time-dependent photoresponse at a constant bias voltage of 10 V (P_{UV} = 2.6 mW, λ = 365nm), in linear and semi-logarithmic scale, respectively.

Figure 3.18 depicts the performance of the sensors when 10 V is applied to their terminals. The 10 V case is thus used as a representative example because it has several similarities to the 5 V case in terms of the finger spacing influence on performance parameters.

Figure 3.18 and Table 3.3, which show the performance parameters of the sensors when 10 V is applied to their terminals, allow us to draw conclusions about the effect of reducing the finger spacing. As such, it is

observed that, just like the ZnO sensors, the I_{ph}, I_{dark}, ΔI, and R_{UV} increase with decreasing spacing. Other ZTO trends, however, contrast with the trends described for the ZnO sensors. Particularly in terms of response times and I_{ph}/I_{dark}. Starting with response times, the τ_{rise} reported for 30 µm sensors is the highest and for the 10 and 50 µm sensors it is almost equal, as shown in Table 3.3. An identical pattern can be seen in the 5 V scenario. As a result, establishing a cause-effect relationship between spacing and τ_{rise} becomes difficult. Recalling the ZnO sensors example, the τ_{rise} and τ_{fall} increased significantly with decreasing spacing. Although the τ_{fall} measured for the ZTO sensors is very similar between spacings, there is a small rise with decreasing spacings. Finally, in terms of the I_{ph}/I_{dark}, it is seen to rise with decreasing spacing, which was the opposite trend verified for ZnO sensors.

It should also be noted that there is some reproducibility in the parameters of 30 µm sensors' three samples (S1, S2, and S3). Especially between S1 and S2, when all parameters have very close values. S3 deviates from the norm by exhibiting an I_{dark} lower than the I_{dark} of the 50 µm sensor, therefore diverging not only in I_{dark} (and, as a result, in the I_{ph}/I_{dark}) but also in τ_{rise}.

Table 3.3: ZTO-based UV sensor parameters obtained as a function of finger spacing of 50, 30 and 10 µm at a fixed applied voltage of 10 V, with one sample for the 50 and 10 µm spacings and three samples for the 30 µm.

		10 V						
Finger Spacing (µm)	***Sample***	t_{rise} **(s)**	t_{fall} **(s)**	I_{ph} **(nA)**	I_{dark} **(nA)**	I_{ph}/I_{dark} **(n.l)**	ΔI **(nA)**	R_{UV} **(µA/W)**
50	***S1***	61	0.9	0.8	0.09	9	0.71	0.27
30	***S1***	94	1.2	1.4	0.12	12	1.28	0.49
	S2	89	1.2	1.3	0.11	12	1.19	0.46
	S3	150	1.2	1.1	0.04	28	1.06	0.41
10	***S1***	65	1.6	17.1	0.41	42	16.7	6.42

A brief comment is included to explain the low I_{ph} reached throughout the ZTO results, which are in the pico and nanoAmpere range. The ZTO NWs not only have a high resistivity (approximately 7.8 kΩ·cm, based on Rovisco's measurement of the NWs arising from this synthesis), but the UV LED radiation employed (E_{LED} = 3.4 eV) is not strong enough to overcome the optical E_g (= 3.89 eV), as previously stated. In other words, the UV radiation is insufficient to excite electrons from the BV to the BC. The I_{ph} formed, on the other hand, may be supported by the fact that the NWs produced although predominantly composed by orth-$ZnSnO_3$ are also composed of a mixture of materials and phases, as well as marked by some defects (as indicated by the PL results) that are responsible for introducing new energy levels between the bands.

3.4.3 UV sensor response to different voltages

The effect of increasing the applied voltage was the same in the three spacings tested. For this reason, the sensor with 10 µm spacing was selected to illustrate and understand this effect. Its performance at an applied voltage of 1, 5 and 10 V is shown in Figure 3.19, with the other two spacings provided in the Annex I.

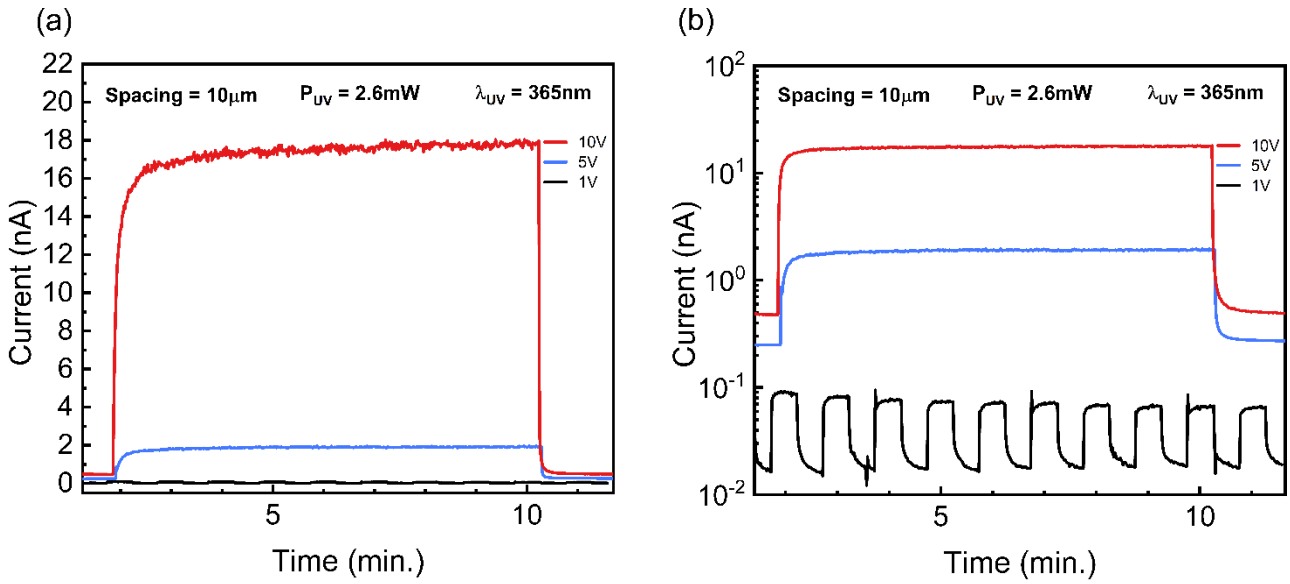

Figure 3.19: (a, b) ZTO-based UV sensor time-dependent photoresponse at different bias voltages of 1, 5 and 10 V in linear and semi-logarithmic scale, respectively.

Table 3.4 shows the parameters of the sensor with 10 µm finger spacing when 1, 5 and 10 V are applied to its terminals. Again, a significant increase in τ_{rise} is observed with increasing applied voltage. It should be remembered that in the case of ZnO, the τ_{rise} increased in the transition from 1 to 5 V but reduced from 5 to 10 V. In terms of the τ_{fall}, it decreases with increasing voltage, which is the opposite of the phenomena found in ZnO sensors. The remaining current related parameters increase with voltage increase, highlighting I_{ph}/I_{dark}, which, as in opposition to what happened with ZnO, also increases with voltage. It should also be emphasized that: the I_{ph} increased from pA to nA during the transition from 1 to 10 V, that the observed increase in I_{dark} is not particularly large, and that R_{UV} increases 320 times.

Table 3.4: ZTO-based UV sensor parameters obtained as a function of an applied voltage of 1, 5 and 10 V for a finger spacing of 10 µm.

		Finger Spacing = 10 µm						
Applied voltage bias (V)	***Sample***	t_{rise} **(s)**	t_{fall} **(s)**	I_{ph} **(nA)**	I_{dark} **(nA)**	I_{ph}/I_{dark} **(n.l)**	ΔI **(nA)**	R_{UV} **(µA/W)**
1	***S1***	3.7	4.4	0.07	0.02	4	0.05	0.02
5	***S1***	38	2.3	1.97	0.25	8	1.72	0.66
10	***S1***	65	1.6	17.1	0.41	42	16.7	6.42

3.4.4 UV illumination power influence

The same tests that were used to investigate the influence of P_{UV} on ZnO sensors, particularly its effect on ΔI, R_{UV}, and S_{UV}, were utilized to evaluate ZTO sensors performance. Chapter 3.3.4 describes these tests and how they were implemented in more detail. The only variation between these tests was the applied voltage, which was 10 V in the case of the ZTO sensors due to the lack of stability at lower voltages.

Figure 3.20 (a) depicts the photocurrent of a ZTO sensor with 10 µm spacing while subjected to various P_{UV}'s, first rising (left half) and then falling (right half). Figure 3.20 (b) depicts the ΔI in one of the ordinate axis and the R_{UV} in the other (both estimated from the right half of Figure 3.20 (a)) as a function of P_{UV}). The S_{UV} is obtained by establishing a linear fit between the ΔI points, which is illustrated by the grey dashed line in Figure 3.20 (b).

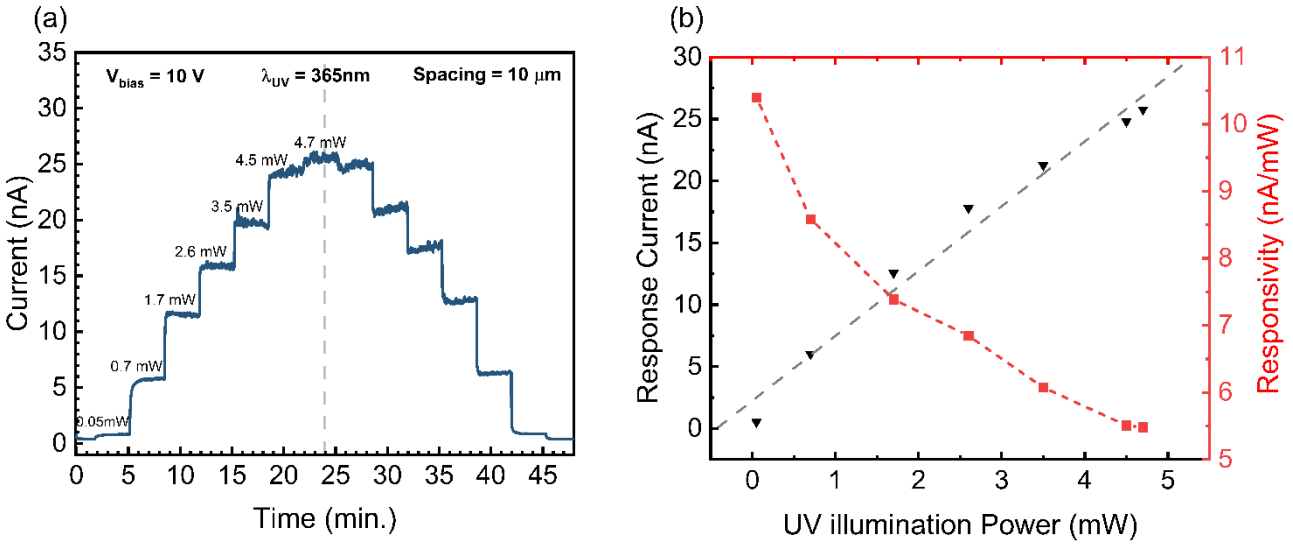

Figure 3.20: (a) ZTO-based UV sensor time-dependent photoresponse to a constant bias voltage of 10 V, increasing the P_{UV} - left half of the graph; and then decreasing the P_{UV} - right half of the graph. (b) ΔI calculated from the right half of (a) as a function of P_{UV}, with the grey dashed line corresponding to the linear fit established between the points of ΔI - which through its slope provides the S_{UV} of the sensor. In the same graph, marked by red square points with a dash red line connecting them, the R_{UV} calculated from (a) is plotted as a function of P_{UV}.

As found for the case of ZnO sensors, we observe the existence of hysteresis patent in Figure 3.20 (a) between the I_{ph} when P_{UV} is rising and when it is falling. The largest difference between ΔI values is 2.04 nA, corresponding to 8.1 % of the sensor span, recorded for the P_{UV} of 2.6 mW. This hysteresis will influence the determination of ΔI and consequently of R_{UV} and S_{UV}. The impact of hysteresis on these parameters is, however, negligible, as can be seen from Figure 3.21, which displays the ΔI of all fingers spacing sensors as well as the corresponding linear fittings as a function of P_{UV}. Table 3.5, which displays the S_{UV} determined for both increasing and decreasing P_{UV} values, supports the same conclusion.

Regarding R_{UV}, there is a decrease in its value with the increase of P_{UV}. This is to be expected, for the same reason evoked for the ZnO example - while the P_{UV} value range comprises three orders of magnitude (from 0.05 to 4.70 mW), the I_{ph} evolution is limited to one order of magnitude on the nA scale.

As for ΔI, it can be observed that it rises as P_{UV} increases, much like ZnO sensors. However, in the case of ZTO, as shown in Figure 3.20 (b), this rise is nearly constant, producing a trajectory that follows the linear fitting obtained from the first to the last ΔI point, giving us a value of S_{UV} equal to (5.24 ± 0.35) nA·mW^{-1}. It is denoted that the sensors with other spacings showed the same type of response to the increase in P_{UV}, as seen in Figure 3.21. It is noted that, the ΔI of 50 and 30 µm sensors were extracted from Figure G.1 b) depicted at Annex G.

As a result, the two S_{UV} regimes previously attributed to ZnO are no longer observed, but only one, illustrating a more constant response to an increase in P_{UV} - i.e., a S_{UV} that does not change significantly depending on the P_{UV} applied. This approximate linear trend reflects the correlation between carrier density and P_{UV} - also seen previously in ZnO sensors.

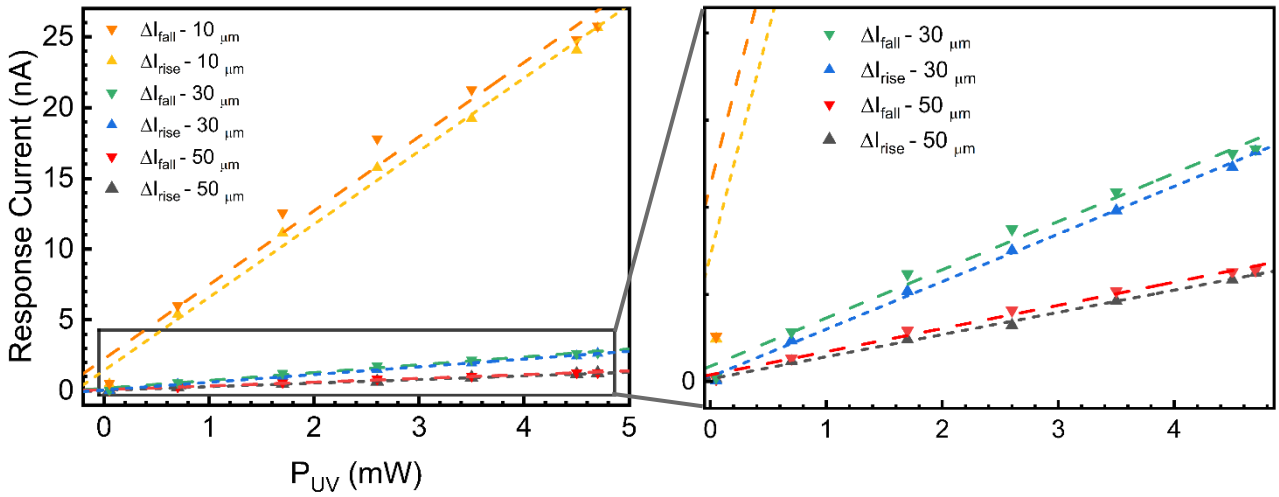

Figure 3.21: ΔI as a function of P_{UV}, calculated from when P_{UV} is rising (ΔI_{rise}) and when it is falling (ΔI_{rise}), with the corresponding linear fittings that reflect the S_{UV}, for the sensors with 50, 30 and 10 µm of finger spacing. The graph on the right shows a zoomed-in section of the 30 and 50 m sensors' ΔI and S_{UV}.

Through Table 3.5 we can see that the smaller the spacing the higher the S_{UV} achieved. Such conclusion is evidenced by Figure 3.21, where it is clear that the slope of the linear fitting of the 10 µm sensor is much steeper than that of the 30 and 50 µm sensors.

Table 3.5: S_{UV} extracted from the linear fittings represented on Figure 3.20 (b) and 3.21, when P_{UV} is falling ($S_{UV\text{-}fall}$) and when it is rising ($S_{UV\text{-}rise}$), as a function of finger spacing for an applied voltage of 10V.

	10 V	
Finger Spacing (µm)	$S_{UV\text{-}fall}$ **(nA·mW^{-1})**	$S_{UV\text{-}rise}$ **(nA·mW^{-1})**
50	0.27	0.25
30	0.56	0.55
10	5.24	5.16

Although no significant increase is observed in the transition between 50 and 30 µm, in the transition from 30 to 10 µm the S_{UV} is increased by approximately 10 times. As the fingers are closer together, there is a greater probability that, through the junction of several NWs, a conductive path is formed between two fingers, and that photogenerated electrons will be collected. Given that the size of the NWs is much smaller than the spacing between fingers, percolation path only occurs through a set of several NWs (at least 10 for a spacing of 10 µm) contacting each other and crossing the distance between two fingers. For then it becomes clear that,

the smaller the distance between fingers the more electrons will be collected (without forgetting that the electric field is stronger and the probability of recombination lower). The same rationale applies to ZnO, however, for the ZTO-based sensors this issue becomes more critical due to the smaller length of the NWs.

3.5 Comparison with the State of the Art

Table 3.6 summarizes some key parameters that describe the photoresponse of ZnO and ZTO-based UV sensors under applied bias of 1 V and 10 V, respectively. The parameters presented in the table are chosen for comparison with other devices reported in the literature.

Table 3.6: Performance parameters of ZnO and ZTO-based UV sensors exposed to a 365 nm UV light (P_{UV} = 2.6 mW) with applied bias of 1 V and 10 V, respectively.

	ZnO-based UV sensor					**ZTO-based UV sensor**				
	1 V (Bias voltage)					**10 V (Bias voltage)**				
Finger Spacing (µm):	t_{rise} **(s)**	t_{fall} **(s)**	I_{ph} **(µA)**	I_{ph}/I_{dark} **(u.l)**	R_{UV} **(mA·W^{-1})**	t_{rise} **(s)**	t_{fall} **(s)**	I_{ph} **(nA)**	I_{ph}/I_{dark} **(u.l)**	R_{UV} **(nA·W^{-1})**
50	43	12	14.5	483	5.6	61	0.9	0.8	9	0.27
30	89	41	27.7	173	11.1	150	1.2	1.1	28	0.49
10	162	30	62.2	63	23.5	65	1.6	17.1	42	6.42

Staring with the ZnO-based UV sensor and comparing it to a ZnO nanorod-based UV sensor reported in reference [24], which employed similar fabrication methods (e.g., hydrothermal synthesis) and used the same interdigitated electrode configuration, our ZnO sensors achieved higher I_{ph}'s considering that the nanorod-based sensor was exposed to a voltage of 2 V and exhibited I_{ph} values in the same µA range as the sensors studied here when exposed to only 1 V. Our sensor also exhibited superior I_{ph}/I_{dark} compared to the nanorod-based sensor, achieving a maximum I_{ph}/I_{dark} of 483, while the nanorod-based sensor only attained a I_{ph}/I_{dark} of 2. However, with regards to the R_{UV}, the nanorod-based sensor exhibited superior performance, displaying higher values (0.19 A·W^{-1} at 2 V) compared to those achieved by the UV sensors fabricated in this study (0.023 A·W^{-1} at 1 V).

ZnO NW-based sensors with the same interdigitated structure fabricated through more expensive high-temperature methods were also compared. Although these sensors achieved higher R_{UV}, such as the sensor reported in reference [25] that reached 10^5 A·W, the I_{ph}'s and I_{ph}/I_{dark}'s obtained by our ZnO sensors were higher (this sensor only reached I_{ph} in the range of nA and a I_{ph}/I_{dark} of only 24.2), and the response times were similar. While the sensor in reference [26] demonstrated much shorter response times (less than 4 s), it should be noted that pristine ZnO nanostructure-based UV sensors generally have long response times, as discussed in a review article [7] that covers the development of ZnO nanostructure-based UV sensors. Various approaches, such as doping ZnO, incorporating noble metal nanoparticles into ZnO NWs to promote localized

surface plasmon resonance effect, or forming ZnO heterojunctions, have been proposed to overcome this limitation.

In summary, the ZnO sensors produced here are competitive with other 1D ZnO nanostructure-based sensors with the same interdigitated electrode configuration, regardless of the fabrication methods. Furthermore, there is still significant potential for improvement in the development of our ZnO-based UV sensor.

Comparisons with other $ZnSnO_3$-based UV sensors are difficult due to the limited number of such sensors reported in the literature. Moreover, the sensors investigated in this work are the first to use solution-based $ZnSnO_3$ NWs as the UV sensing material. As shown in Table 3.6, when the developed ZTO sensors were exposed to a 365 nm wavelength and a 10 V bias voltage, they exhibited a t_{rise} between 60 and 150 s, a t_{fall} between 0.9 and 1.6 s, a maximum I_{ph} of 17.1 nA, a maximum I_{ph}/I_{dark} of 42, and a maximum R_{UV} of 6.42 $nA \cdot W^{-1}$.

A comparison was made between UV sensors based on $ZnSnO_3$ nanostructures synthesized using high-temperature methods, as the few sensors of this type reported in the literature have employed this approach. Referring to the $ZnSnO_3$ nanostructure-based UV sensors discussed in the Introduction chapter, one using a single $ZnSnO_3$ NW [37] and the other using $ZnSnO_3$ cubic nanoparticles [38], it is evident that both I_{ph} and I_{ph}/I_{dark} are much higher even when exposed to a 3 V bias voltage. The single NW sensor achieved I_{ph} values in the hundreds of nA range, while the cubic nanoparticle achieved I_{ph}'s in the µA range. The corresponding I_{ph}/I_{dark} were approximately 800 and 10^3, respectively. These better results are attributed to high-temperature methods that included thermal post-treatments and the use of Au electrodes. As previously discussed, such methods that promote a defect-free crystalline structure can significantly improve the photoresponse of nanostructures. The better performance of the single NW sensor can also be attributed to the fact that it was exposed to a lower UV radiation of 300 nm. However, it should be noted that these two sensors have much lower t_{rise} (around 20s), but a much higher t_{fall} (around 60s compared to our maximum of 1.6 s). Moreover, these two sensors used reduced UV exposure times that did not allow I_{ph} to saturate and which in turn indicated unstable behavior.

In summary, while the performance of the sensors presented here does not surpass the literature on $ZnSnO_3$-based UV sensors, they are manufactured using simpler, low-temperature methods and more affordable materials. Furthermore, despite being subject to higher voltages, the sensors presented here demonstrated more stable behavior. Finally, there is still significant potential for further improvement in the sensors developed in this work.

4 Conclusions and Future Perspectives

In this work, it is reported the successful fabrication and characterization of UV sensors based on NWs synthesized using solution-based methods of two metal oxides, namely $ZnSnO_3$ and ZnO. While ZnO has been extensively studied for UV sensing, $ZnSnO_3$ has received relatively less attention for this application. In this sense, it is emphasized that this work represents the first use of solution-synthesized $ZnSnO_3$ NWs for UV sensing.

The $ZnSnO_3$ NWs hydrothermally synthesized acted as the active layer of the sensors. These ZTO-based UV sensors demonstrated a promising response to UV radiation, with a S_{UV} of 5.2 nA·mW^{-1}, R_{UV} of 6.42 µA·mW^{-1}, and I_{ph}/I_{dark} of 42 (under the conditions of 10 V applied bias for a finger spacing of 10 µm, and UV radiation at 365 nm). The sensors developed in this work offer a simpler and more cost-effective alternative to the literature on $ZnSnO_3$-based UV sensors. Although their performance does not surpass the state-of-the-art, they exhibit more stable behavior when subjected to higher voltages (> 5 V). Nonetheless, there is still considerable potential for further improvement.

ZnO-based sensors, produced via a 5-min. MW-assisted hydrothermal synthesis, were tested and demonstrated a good UV response, providing additional insights into the results obtained from the ZTO-based sensors. Notably, the photoresponse was characterized by a S_{UV} of 13.4 µA·mW^{-1} for low P_{UV} levels (between 0.05 and 0.7 mW), a R_{UV} of 5.6 mA·mW^{-1}, and an I_{ph}/I_{dark} of 483 (under the conditions of 1 V applied bias for a finger spacing of 50 µm and UV radiation at 365 nm). Overall, the results demonstrate that the ZnO sensors developed in this study demonstrated competitive performance compared to other 1D pristine ZnO nanostructure-based sensors with similar interdigitated electrode configurations. Additionally, the sensors exhibited promising potential for further optimization and improvement.

The characterization of both types of sensors was performed by studying the effect of applied voltage, finger spacing, and UV light power, allowing for a better understanding of the nanostructures UV response by tracking the evolution of the parameters that describe their performance.

- **Finger Spacing influence:**

For the ZnO and ZTO-based sensors, tests were conducted using finger spacings of 50, 30, and 10 µm. It was observed that a smaller distance between the fingers resulted in higher I_{ph} generation. This can be attributed to the reduced distance that photocarriers have to travel before being collected, as well as the formation of a stronger electric field, which facilitates the separation and collection of photocarriers and reduces the probability of recombination. Furthermore, it was found that I_{dark} increased as finger spacing decreased for both ZnO and ZTO sensors. However, this increase did not prevent the increase of ΔI and R_{UV}. In the case of ZnO, the increase in I_{dark} resulted in a decrease in I_{ph}/I_{dark}. Conversely, ZTO sensors demonstrated an increase in I_{ph}/I_{dark} with decreasing finger spacing, indicating a highly promising feature of this ZTO NWs for UV sensing applications. However, the I_{ph} generated by ZTO sensors is significantly lower than that of ZnO sensors. This can be attributed to the high E_g of ZTO (E_g = 3.89 eV) and the high resistivity of its NWs (approximately 7.8 kΩ·cm). As for the response times, it is evident that decreasing the spacing between fingers in ZnO sensors results in a considerable increase in both t_{rise} and t_{fall}. In contrast, establishing a relationship between spacing and response time for ZTO sensors is more challenging. Although a slight increase in t_{fall} was observed for smaller spacings, the t_{rise} for ZTO sensors was higher for the 30 µm sensor and relatively similar for the 10 and 50 µm sensors. Despite this, both ZnO and ZTO sensors exhibited very long response times. ZnO sensors exhibited t_{rise} values of over 1 min. and t_{fall} values of approximately 40 s, while ZTO sensors exhibited long t_{rise} values of over 1 min. but displayed a short t_{fall} of around 1 s.

The PL analysis of both ZnO and ZTO NWs revealed the presence of numerous defects especially in the form of oxygen vacancies. These defects, as supported by the literature and the presented results, have a

strong negative impact on the photoresponse. UV sensors with the same interdigital configuration were fabricated using a ZnO thin film as the active layer. Although the structure is not nanostructured, a thin film deposited by sputtering can exhibit fewer defects (theoretically) and was found to produce much lower response times (t_{rise} of around 20 s and t_{fall} of 0.79 s) and a much higher I_{ph}/I_{dark} (> 10^3).

- **Applied voltage influence:**

To investigate the impact of voltage on the sensors UV response, the spacing between fingers was held constant while 1, 5 and 10 V were applied to their terminals. The results indicate that increasing the voltage and decreasing the finger spacing have similar effects, as both lead to an increase in the electric field. For both ZnO and ZTO-base sensors, an increase in applied voltage generated higher I_{ph} and I_{dark}, resulting in higher ΔI and R_{UV}. Notably, the I_{ph}/I_{dark} decreased for ZnO, while increased for ZTO. It is worth mentioning that, in the case of ZTO alone, an applied bias of 1 V was insufficient to produce a stable UV response. In this case, multiple oscillations in the generated I_{ph}, (in the order of pA), were observed primarily for spacings of 50 and 30 µm. A more stable behavior was then observed at higher voltages of 5 and 10 V. Regarding response times, increasing the applied voltage led to a significant increase in t_{fall} and t_{rise} for ZnO sensors. However, it should be noted that an increase in t_{rise} only occurred between 1 and 10 V voltages. Between 5 and 10 V, t_{rise} decreased slightly. In contrast, ZTO sensors showed a decrease in t_{fall} and an increase in t_{rise}, with increasing voltage.

- **UV illumination power influence - S_{UV} extraction:**

The study on the effect of varying the P_{UV} on NWs was crucial in determining the S_{UV} and in gaining a better understanding of how the intensity of the UV signal impacts the variation in ΔI and R_{UV}. Briefly, an increase P_{UV} resulted in a decrease in R_{UV} and an increase in ΔI. However, the growth and evolution of ΔI differed between the two sensor types. Specifically, for ZnO sensors, a more abrupt growth was observed at lower powers followed by a more gradual increase, identifying two S_{UV} regimes. On the other hand, ZTO sensors showed a more constant growth throughout the tested P_{UV}'s, identifying a single S_{UV} regime. It is also noteworthy that, having performed these tests for the various spacings, a significant increase in S_{UV} was observed with decreasing spacing.

- **Reproducibility:**

Despite efforts to achieve reproducibility of the devices, the utilization of drop-casting method for NW dispersion resulted in some limitations. However, a notable degree of similarity was observed between the replicated devices, particularly in the ZTO sensors.

- **Future Perspectives:**

To improve the performance of UV sensors based on ZTO and ZnO NWs, various avenues of research can be pursued. One promising approach is to implement a post-thermal treatment for $ZnSnO_3$ NWs to mitigate defects and adjust their E_g to lower values. Similarly, a hydrothermal treatment (mentioned in the results chapter) can be performed to reduce the concentration of oxygen vacancies in ZnO NWs. To further enhance the UV sensor performance, reducing the spacing between the interdigitated fingers to the nanometer scale and exploring new geometries, such as the finger area or finger thickness, are also recommended. Furthermore, new deposition methods, including NW alignment methods, should be investigated to improve sensor performance and reproducibility.

To enable a more comprehensive characterization of the UV sensors, it is recommended to measure additional P_{UV} values, with a particular focus on values between 0.05 and 0.7 mW. Additionally, studying the spectral response of the sensors by testing their photoresponse under different wavelengths is strongly suggested. In order to assess the long-term stability of the UV sensors, it is suggested that future tests involve subjecting these sensors to a significant number of cycles over several consecutive hours. Furthermore, it is proposed that a larger number of sensor samples be replicated to obtain more conclusive results regarding reproducibility.

5 References

[1] Pang C, Yan B, Liao L, Liu B, Zheng Z, Wu T, Sun H and Yu T 2010 Synthesis, characterization and opto-electrical properties of ternary Zn2SnO4 nanowires *Nanotechnology* **21**

[2] Theerthagiri J, Salla S, Senthil R A, Nithyadharseni P, Madankumar A, Arunachalam P, Maiyalagan T and Kim H S 2019 A review on ZnO nanostructured materials: Energy, environmental and biological applications *Nanotechnology* **30**

[3] Baruah S and Dutta J 2011 Zinc stannate nanostructures: Hydrothermal synthesis *Sci Technol Adv Mater* **12**

[4] Rovisco A, Branquinho R, Martins J, Oliveira M J, Nunes D, Fortunato E, Martins R and Barquinha P 2018 Seed-layer free zinc tin oxide tailored nanostructures for nanoelectronic applications: Effect of chemical parameters *ACS Appl Nano Mater* **1** 3986–97

[5] Rovisco A, Branquinho R, Martins J, Fortunato E, Martins R and Barquinha P 2019 Growth mechanism of seed-layer free ZnSnO3 nanowires: effect of physical parameters *Nanomaterials* **9**

[6] Sang L, Liao M and Sumiya M 2013 A comprehensive review of semiconductor ultraviolet photodetectors: From thin film to one-dimensional nanostructures *Sensors* **13** 10482–518

[7] Deka Boruah B 2019 Zinc oxide ultraviolet photodetectors: Rapid progress from conventional to self-powered photodetectors *Nanoscale Adv* **1** 2059–85

[8] Nunes D, Pimentel A, Gonçalves A, Pereira S, Branquinho R, Barquinha P, Fortunato E and Martins R 2019 Metal Oxide Nanostructures for Sensor Applications *Semicond Sci Technol* 0–22

[9] Alaie Z, Nejad S M and Yousefi M H 2015 Recent advances in ultraviolet photodetectors *Mater Sci Semicond Process* **29** 16–55

[10] Zhai T, Fang X, Liao M, Xu X, Zeng H, Yoshio B and Golberg D 2009 A comprehensive review of one-dimensional metal-oxide nanostructure photodetectors *Sensors* **9** 6504–29

[11] Zou Y, Zhang Y, Hu Y and Gu H 2018 Ultraviolet detectors based on wide bandgap semiconductor nanowire: A review *Sensors* **18**

[12] Bashir S and Liu J L 2015 Nanomaterials and Their Application *Advanced Nanomaterials and Their Applications in Renewable Energy* (Elsevier Inc.) pp 1–50

[13] Shen G and Chen D 2010 *One-Dimensional Nanostructures for Photodetectors* vol 4

[14] Soci C, Zhang A, Xiang B, Dayeh S A, Aplin D P R, Park J, Bao X Y, Lo Y H and Wang D 2007 ZnO nanowire UV photodetectors with high internal gain *Nano Lett* **7** 1003–9

[15] Ferreira S H, Cunha I, Pinto J V, Neto J P, Pereira L, Fortunato E and Martins R 2021 Uv-responsive screen-printed porous zno nanostructures on office paper for sustainable and foldable electronics *Chemosensors* **9**

[16] Cammi D and Ronning C 2014 Persistent photoconductivity in ZnO nanowires in different atmospheres *Advances in Condensed Matter Physics* **2014**

[17] Liu K, Sakurai M and Aono M 2010 ZnO-based ultraviolet photodetectors *Sensors* **10** 8604–34

[18] Li X, Liu X, Li Y, Gao D and Cao L 2021 Using Novel Semiconductor Features to Construct Advanced ZnO Nanowires-Based Ultraviolet Photodetectors: A Brief Review *IEEE Access* **9** 11954–73

[19] Pimentel A, Samouco A, Nunes D, Araújo A, Martins R and Fortunato E 2017 Ultra-fast microwave synthesis of ZnO nanorods on cellulose substrates for UV sensor applications *Materials* **10**

[20] Panda S K and Jacob C 2012 Preparation of transparent ZnO thin films and their application in UV sensor devices *Solid State Electron* **73** 44–50

[21] Samouco A, Marques A C, Pimentel A, Martins R and Fortunato E 2018 Laser-induced electrodes towards low-cost flexible UV ZnO sensors *Flexible and Printed Electronics* **3**

[22] Wang Z L 2004 Zinc oxide nanostructures: Growth, properties and applications *Journal of Physics Condensed Matter* **16**

[23] Henary M, Kananda C, Rotolo L, Savino B, Owens E A and Cravotto G 2020 Benefits and applications of microwave-assisted synthesis of nitrogen containing heterocycles in medicinal chemistry *RSC Adv* **10** 14170–97

[24] Singh S, Kumar Y, Kumar H, Vyas S, Periasamy C, Chakrabarti P, Jit S and Park S H 2017 A study of hydrothermally grown ZnO nanorod-based metal-semiconductor-metal UV detectors on glass substrates *Nanomaterials and Nanotechnology* **7**

[25] Mallampati B, Nair S V, Ruda H E and Philipose U 2015 ZnO Nanowire Based Photoconductor with High Photoconductive Gain *Mater. Res. Soc. Symp. Proc* **1** 5

[26] Alsultany F H, Hassan Z and Ahmed N M 2016 A high-sensitivity, fast-response, rapid-recovery UV photodetector fabricated based on catalyst-free growth of ZnO nanowire networks on glass substrate *Opt Mater (Amst)* **60** 30–7

[27] Rovisco A, Branquinho R, Pinto J V, Martins R, Fortunato E and Barquinha P 2020 Hydrothermal Synthesis of Zinc Tin Oxide Nanostructures for Photocatalysis, Energy Harvesting and Electronics *Novel Nanomaterials* (IntechOpen)

[28] Rovisco A, Barquinha P and Branquinho R 2019 *Solution-based Zinc-Tin Oxide nanostructures: from synthesis to applications. Dissertação para obtenção do Grau de Doutor em Nanotecnologias e Nanociências*

[29] Nalimova S S, Maksimov A I, Matyushkin L B and Moshnikov V A 2019 Current State of Studies on Synthesis and Application of Zinc Stannate (Review) *Glass Physics and Chemistry* **45** 251–60

[30] Kim T G, Shin D S and Park J 2016 Investigation of crystallized ZnSnO3 nanoparticles for ultraviolet photodetectors *J Nanosci Nanotechnol* **16** 10272–5

[31] Liu C, Piyadasa A, Piech M, Dardona S, Ren Z and Gao P X 2016 Tunable UV response and high performance of zinc stannate nanoparticle film photodetectors *J Mater Chem C Mater* **4** 6176–84

[32] Rovisco A, Branquinho R, Deuermeier J, Freire T, Fortunato E, Martins R and Barquinha P 2021 Shape Effect of Zinc-Tin Oxide Nanostructures on Photodegradation of Methylene Blue and Rhodamine B under UV and Visible Light *ACS Appl Nano Mater* **4** 1149–61

[33] Rovisco A, Dos Santos A, Cramer T, Martins J, Branquinho R, Águas H, Fraboni B, Fortunato E, Martins R, Igreja R and Barquinha P 2020 Piezoelectricity Enhancement of Nanogenerators Based on PDMS and ZnSnO3Nanowires through Microstructuration *ACS Appl Mater Interfaces* **12** 18421–30

[34] Zhao Y, Hu L, Liu H, Liao M, Fang X and Wu L 2014 Band gap tunable Zn2SnO4 nanocubes through thermal effect and their outstanding ultraviolet light photoresponse *Sci Rep* **4**

[35] Dong Y, Wang S, Zou Y, Liu S, Zhu Z, Li J, Ju D, Chen J, Zhang K, Liu X and Zeng H 2018 Zinc Stannate Nanocrystal–Based Ultrarapid-Response UV Photodetectors *Adv Mater Technol* **3**

[36] Zhang Y, Wang J, Zhu H, Li H, Jiang L, Shu C, Hu W and Wang C 2010 High performance ultraviolet photodetectors based on an individual Zn 2SnO4 single crystalline nanowire *J Mater Chem* **20** 9858–60

[37] Wu J M, Hsu G K, Yeh H-H and Lin H-C 2012 Metallic Zinc Nanowires Effect in High-Performance Photoresponsive and Photocatalytic Properties of Composite Zinc Stannate Nanowires *J Electrochem Soc* **159** H497–501

[38] Wang X, Xia M, Li H, Zhu X, Leng B, Tao T, Xu W and Xu J 2019 Preparation of transparent amorphous ZnSnO3 cubic nanoparticles and light-induced homostructures: Application in UV sensor and room-temperature gas sensor *Appl Surf Sci* **493** 862–72

[39] Rasool A, Santhosh Kumar M C, Mamat M H, Gopalakrishnan C and Amiruddin R 2020 Analysis on different detection mechanisms involved in ZnO-based photodetector and photodiodes *Journal of Materials Science: Materials in Electronics* **31** 7100–13

[40] Al-Hardan N H, Hamid M A A, Shamsudin R and Othman N K 2017 Ultraviolet Sensors Based on Two-Dimensional Zinc Oxide Structures *Optoelectronics - Advanced Device Structures* (InTech)

[41] Abdulrahman A F, Ahmed S M, Barzinjy A A, Hamad S M, Ahmed N M and Almessiere M A 2021 Fabrication and characterization of high-quality uv photodetectors based zno nanorods using traditional and modified chemical bath deposition methods *Nanomaterials* **11** 1–26

[42] Michael J Mcgrath and Cliodhna Ni Scanaill 2013 *Sensing and Sensor Fundamentals What Is a Sensor and What Is Sensing?*

[43] Pimentel A, Nunes D, Duarte P, Rodrigues J C, Mendes Costa F, Monteiro T, Ferrão de Paiva Martins R and Fortunato E 2014 Synthesis of Long ZnO Nanorod under Microwave Irradiation or Conventional Heating Synthesis of Long ZnO Nanorods under Microwave Irradiation or Conventional Heating *J. Phys. Chem. C* 12

[44] Cullity B D (Bernard D 1978 *Elements of x-ray diffraction* (Addison-Wesley Publishing Company, Inc)

[45] Aljaafari A, Ahmed F, Awada C and Shaalan N M 2020 Flower-Like ZnO Nanorods Synthesized by Microwave-Assisted One-Pot Method for Detecting Reducing Gases: Structural Properties and Sensing Reversibility *Front Chem* **8**

[46] Pimentel A, Rodrigues J, Duarte P, Nunes D, Costa F M, Monteiro T, Martins R and Fortunato E 2015 Effect of solvents on ZnO nanostructures synthesized by solvothermal method assisted by microwave radiation: a photocatalytic study *J Mater Sci* **50** 5777–87

[47] Ferreira S H, Morais M, Nunes D, Oliveira M J, Rovisco A, Pimentel A, Águas H, Fortunato E and Martins R 2021 High UV and sunlight photocatalytic performance of porous ZnO nanostructures synthesized by a facile and fast microwave hydrothermal method *Materials* **14**

[48] Musa I, Qamhieh N and Mahmoud S T 2017 Synthesis and length dependent photoluminescence property of zinc oxide nanorods *Results Phys* **7** 3552–6

[49] Samavati A, Awang A, Samavati Z, Fauzi Ismail A, Othman M H D, Velashjerdi M, Eisaabadi B. G and Rostami A 2021 Influence of ZnO nanostructure configuration on tailoring the optical bandgap: Theory and experiment *Mater Sci Eng B Solid State Mater Adv Technol* **263**

[50] Sáenz-Trevizo A, Amézaga-Madrid P, Pizá-Ruiz P, Antúnez-Flores W and Miki-Yoshida M 2016 Optical band gap estimation of ZnO nanorods *Materials Research* vol 19 (Universidade Federal de Sao Carlos) pp 33–8

[51] Rodrigues J, Ben Sedrine N, Correia M R and Monteiro T 2020 Photoluminescence investigations of ZnO micro/nanostructures *Mater Today Chem* **16**

[52] Han F, Yang S, Jing W, Jiang K, Jiang Z, Liu H and Li L 2014 Surface plasmon enhanced photoluminescence of ZnO nanorods by capping reduced graphene oxide sheets *Opt Express* **22** 11436

[53] Liu J P, Xu C X, Zhu G P, Li X, Cui Y P, Yang Y and Sun X W 2007 Hydrothermally grown ZnO nanorods on self-source substrate and their field emission *J Phys D Appl Phys* **40** 1906–9

[54] Jeon S M, Kim M S, Cho M Y, Choi H Y, Yim K G, Kim G S, Kim H G, Leem J Y, Lee D Y, Kim J S, Kim J S and Lee J I 2010 Fabrication of porous ZnO nanorods with nano-sized pores and their properties *Journal of the Korean Physical Society* **57** 1477–81

[55] Tzeng S K, Hon M H and Leu I C 2013 Suppressing the atmosphere-induced performance instability of solution-grown zinc oxide-nanowire ultra-violet photodetector by hydrothermal treatment in water *Mater Chem Phys* **139** 963–7

[56] Saafi I, Dridi R, Mimouni R, Amlouk A, Yumak A, Boubaker K, Petkova P and Amlouk M 2016 Microstructural and optical properties of SnO2-ZnSnO3 ceramics *Ceram Int* **42** 6273–81

[57] Dabbabi S, Nasr T Ben, Madouri A, Cavanna A, Garcia-Loureiro A and Kamoun N 2019 Fabrication and Characterization of Sensitive Room Temperature NO2 Gas Sensor Based on ZnSnO3 Thin Film *Physica Status Solidi (A) Applications and Materials Science* **216**

[58] Wang Y, Gao P, Bao D, Wang L, Chen Y, Zhou X, Yang P, Sun S and Zhang M 2014 One pot, two phases: Individual orthorhombic and face-centered cubic ZnSnO3 obtained synchronously in one solution *Inorg Chem* **53** 12289–96

[59] Zheng J, Hou H, Fu H, Gao L and Liu H 2021 Size-controlled synthesis of porous ZnSnO3nanocubes for improving formaldehyde gas sensitivity *RSC Adv* **11** 20268–77

[60] Wang D, Pu X, Yu X, Bao L, Cheng Y, Xu J, Han S, Ma Q and Wang X 2022 Controlled preparation and gas sensitive properties of two-dimensional and cubic structure ZnSnO3 *J Colloid Interface Sci* **608** 1074–85

[61] Landi S, Segundo I R, Freitas E, Vasilevskiy M, Carneiro J and Tavares C J 2022 Use and misuse of the Kubelka-Munk function to obtain the band gap energy from diffuse reflectance measurements *Solid State Commun* **341**

[62] Akir S, Barras A, Coffinier Y, Bououdina M, Boukherroub R and Omrani A D 2016 Eco-friendly synthesis of ZnO nanoparticles with different morphologies and their visible light photocatalytic performance for the degradation of Rhodamine B *Ceram Int* **42** 10259–65

Annexes

Annex A – Steps involved in the UV sensors fabrication process

Figure A.1 presents a schematic illustration of the sequential steps involved in the fabrication process of UV sensors. All the steps were identical for both ZnO and ZTO-based sensors, except for the absence of step C) in the fabrication process of ZTO devices.

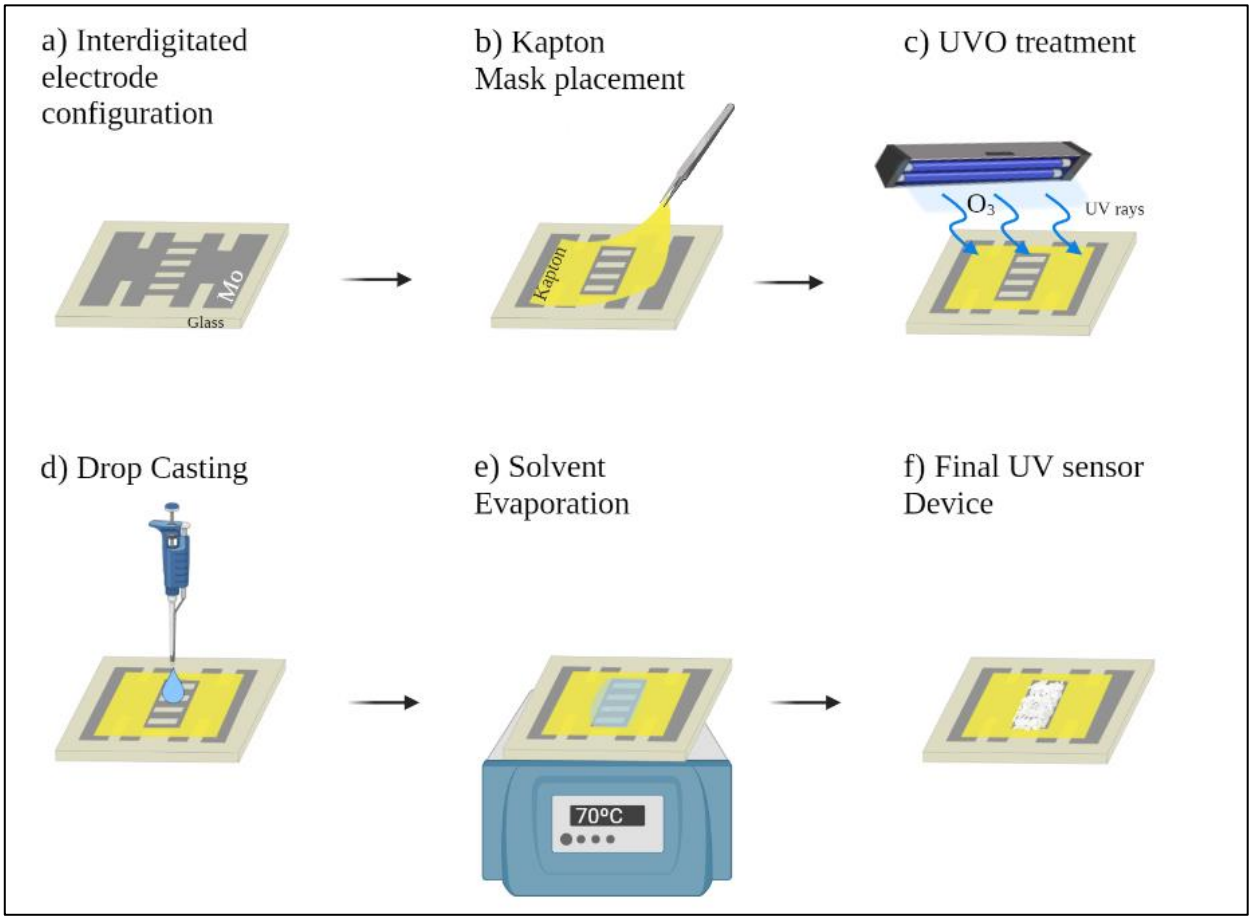

Figure A.1: Process flow for the fabrication of UV sensors, depicting the sequential steps involved in the fabrication process.

Annex B – Images of the UV sensors fabricated

Figure B.1 a) depicts an image of the interdigitated electrode configuration employed in the fabrication of the UV sensors. Additionally, Figures B.1 b) and B.1 c) depict an example of ZnO and ZTO-based UV sensors along with magnified images of the deposited NWs in the central region of the finger area, obtained using an optical microscope. The observed NW distribution pattern in the magnified images suggests a random display and the formation of agglomerates. To obtain more conclusive results, it is essential to observe the NWs using SEM.

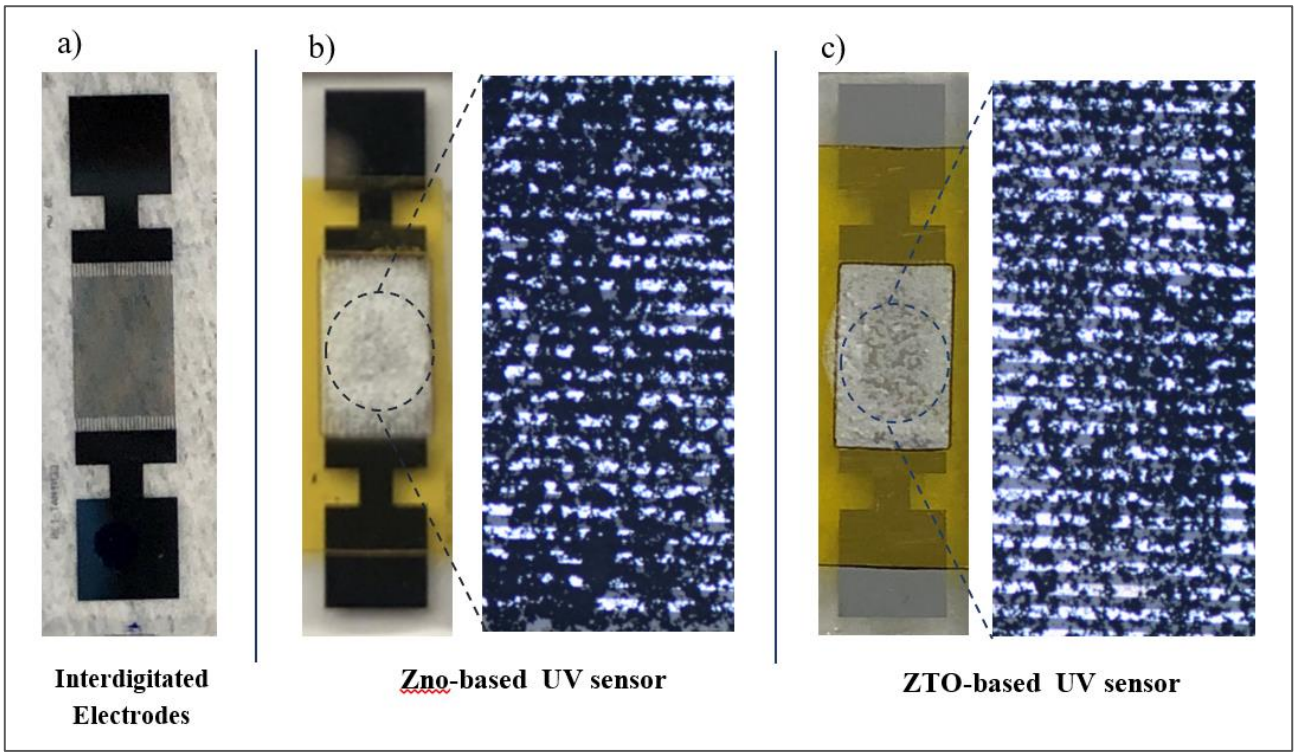

Figure B.1: a) Image of the Mo interdigitated electrode configuration used to fabricate UV sensors. b) Image of a ZnO-based UV sensor, with a magnified view of the central region of the finger area where ZnO NWs are dispersed. c) Image of a ZTO-based UV sensor, with a magnified view of the central region of the finger area where ZTO NWs are dispersed.

Annex C – Demonstration of the Kubleka-Munk Method

The E_g was calculated using the Kubelka-Munk (K-M) method applied to the reflectance (R) data. Assuming a sample of semi-infinite thickness, the K-M function is described as follows [61]:

$$F(R) = \frac{K}{S} = \frac{(1-R)^2}{2R} \tag{5}$$

where K and S are the K-M absorption and scattering coefficients, respectively.

The following expressions are presented in order to reach a final one that was used to determine the E_g as will be explained further. For semiconductors, the principal absorption mechanism is due to interband transitions, and the absorption coefficient (α) can be written in the following form [61]:

$$\alpha(E) \propto \frac{(E - E_g)^p}{E}, \tag{6}$$

where E is the photon energy, and the exponent p is a constant that depends on the band structure of the semiconductor (p = 2 for direct bandgap semiconductors).

Known that K and S ratio are proportional to intrinsic absorption and scattering (s) coefficients ratio, we can write [61]:

$$\frac{K}{S} \propto \frac{\alpha}{s} \tag{7}$$

And considering the power-law energy dependence of the scattering coefficient as [61]:

$$s \propto E^q \tag{8}$$

where q = 2 or 4, depending on the relation between characteristic scale of the inhomogeneities and the E wavelength (λ).

F(R) can be expressed through its relation between α (eq. 6 and 7) and the power-law energy dependence of the *s* coefficient (eq. 8) [61]:

$$F(R) \propto \frac{(E - E_g)^p / E}{E^q} \tag{9}$$

Since in the vicinity of the E_g it is possible to approximate E^q for a constant, neglecting the scattering effect (S and s), we can write the following expression [61]:

$$(F(R) \times E)^{\frac{1}{p}} = A(E - E_g) \tag{10}$$

Finally, through eq. 10, E_g was obtained by extrapolating to zero a linear fit to a plot of $(F(R)\times E)^{1/p}$ versus E, as shown in Figure 3.4 (b) and 3.10 (b), in the Results chapter [61,62].

Annex D – ZnO thin-film UV sensor by sputtering

The time-dependent photoresponse of the UV sensor with a ZnO thin film (with 50 nm of thickness) deposited via sputtering, when subjected to 1, 5 and 10 V, is depicted in Figure D.1. The testing conditions used in this study were the same as those employed to characterize the sensors based on nanostructures. Notably, the thin film is confined to the finger region, similar to the nanostructure-based sensors shown at Annex B. Table D.1 reports the parameters extracted from Figure D.1. Despite the low currents obtained, on the nA scale, the response times are significantly shorter and the I_{ph}/I_{dark} are substantially higher (>10^3) . Comparing the results with those of ZnO-based UV sensors, we can infer that the observed improvements are partially attributed to the theoretically lower defect density of thin films. These results suggest that the UV response of ZnO and ZTO NW-based sensors could be enhanced by mitigating their structural defects.

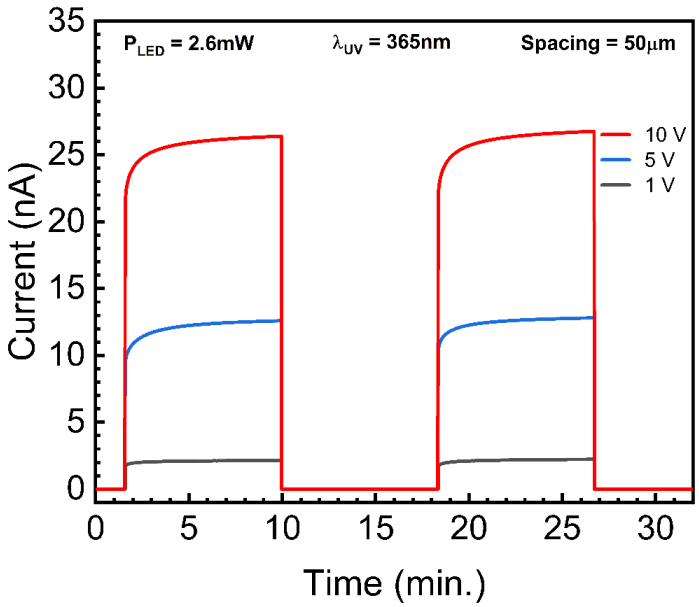

Figure D.1: Time-dependent photoresponse at different bias voltages of 1, 5 and 10V.

Table D.1: UV sensor parameters obtained as a function of an applied voltage of 1, 5 and 10 V for a finger spacing of 10 µm.

		Finger Spacing = 50 µm						
Applied voltage bias (V)	***Sample***	t_{rise} **(s)**	t_{fall} **(s)**	I_{ph} **(nA)**	I_{dark} **(nA)**	I_{ph}/I_{dark} **(u.l)**	ΔI **(nA)**	R_{UV} **(µA/W)**
1	***S1***	22	0.79	2.2	$3.5 \cdot 10^{-4}$	$6 \cdot 10^{3}$	2.2	0.82
5	***S1***	21	0.79	12.6	$4.3 \cdot 10^{-4}$	$3 \cdot 10^{4}$	12.6	4.83
10	***S1***	19	0.79	26.8	$5.2 \cdot 10^{-4}$	$6 \cdot 10^{4}$	26.8	10.3

Annex E – Finger Spacing influence on ZnO-based UV sensors under 5 V and 10 V of applied voltage:

Figure E.1 (a) and (b) show the time-dependent photoresponse of the 50 and 30 µm ZnO-based UV sensors when subjected to 5 and 10 V, respectively. Table E.1 displays the respective parameters that were determined from Figure E.1 (a) and (b) and allow to conclude that the finger spacing influence between the three applied voltage tested (1, 5 and 10 V) was very similar.

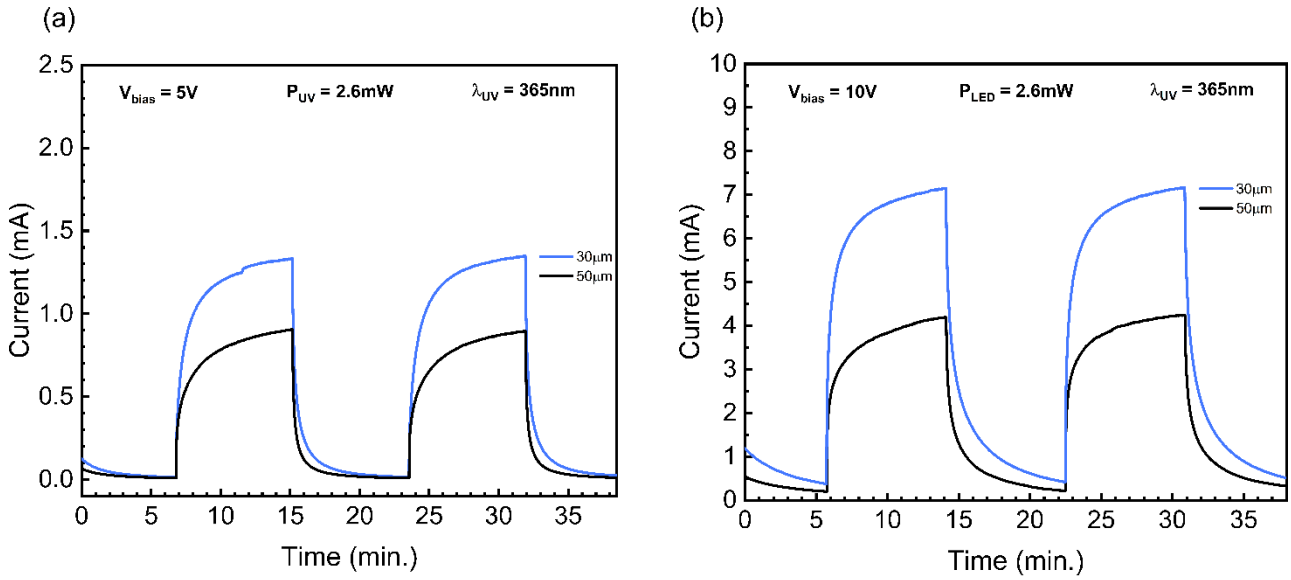

Figure E.1: (a) ZnO-based UV time-dependent photoresponse at a constant bias voltage of 5V (b) and 10V, (P_{UV} = 2.6 mW, λ = 365nm). Lines depicting the performance of the 30 µm sensors are in blue and 50 µm sensors in black.

Table E.1: ZnO-based UV sensor parameters obtained as a function of finger spacing of 50 and 30 µm at a fixed applied voltage of 5 V and 10 V.

		5 V						
Finger Spacing (µm)	***Sample***	t_{rise} **(s)**	t_{fall} **(s)**	I_{ph} **(mA)**	I_{dark} **(µA)**	I_{ph}/I_{dark} **(u.l)**	ΔI **(mA)**	R_{UV} **(A/W)**
50	***S1***	228	62	0.91	9	96	0.90	0.34
30	***S1***	174	88	1.34	15	89	1.33	0.51
		10 V						
Finger Spacing (µm)	***Sample***	t_{rise} **(s)**	t_{fall} **(s)**	I_{ph} **(mA)**	I_{dark} **(mA)**	I_{ph}/I_{dark} **(u.l)**	ΔI **(mA)**	R_{UV} **(A/W)**
50	***S1***	172	156	4.24	0.22	19	4.02	1.54
30	***S1***	154	191	7.15	0.42	17	6.73	2.58

Annex F – Applied voltage influence on ZnO-based UV sensor with 30µm of finger spacing:

Figure F.1 illustrates the time-dependent photoresponse of ZnO-based UV sensors with a spacing of 30 µm when subjected to 1, 5 and 10 V. As presented in Table F.1, which summarizes the parameters extracted from Figure F.1, the impact of voltage variation on the UV sensor's performance is identical to that of the 50 µm sensor. Both currents (I_{ph} and I_{dark}) increase as the spacing decreases, leading to an increase in ΔI and R_{UV}, albeit with a decrease in I_{ph}/I_{dark}. Conversely, the response times rise as the spacing decreases. That is, the same trends are repeated. These observations support the notion that the effect of voltage on the sensor's performance is independent of the spacing.

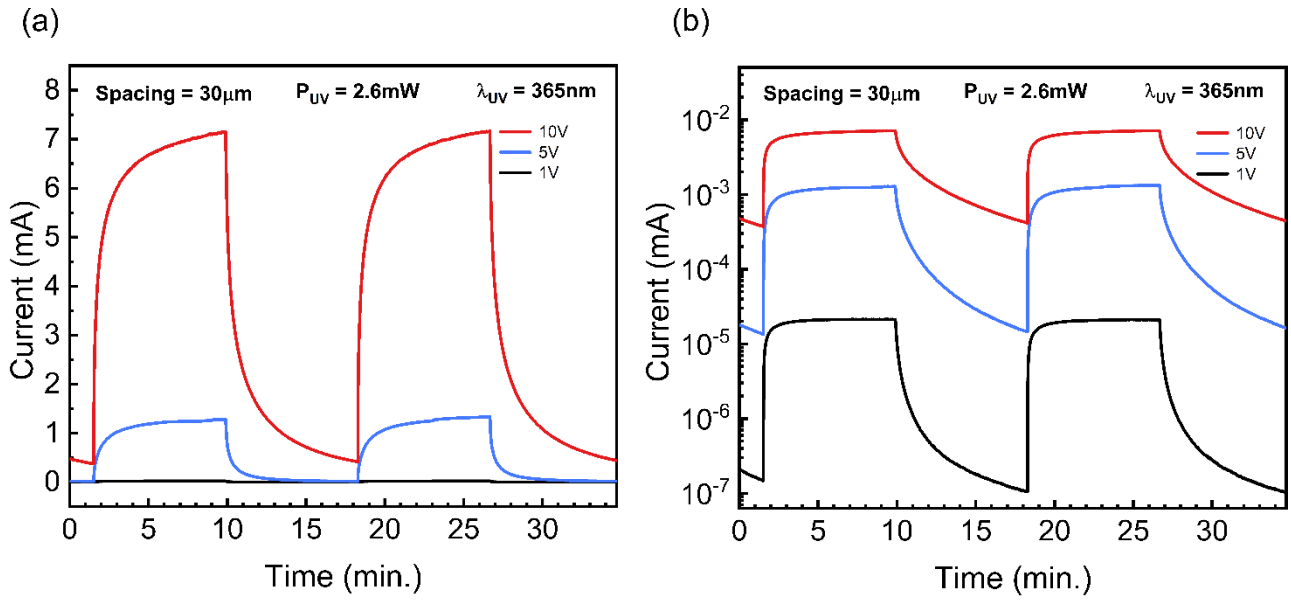

Figure F.1: (a, b) ZnO-based UV sensor time-dependent photoresponse at different bias voltages of 1, 5 and 10V in a linear and semi-logarithmic scale, respectively.

Table F.1: ZnO-based UV sensor parameters obtained as a function of an applied voltage of 1, 5 and 10 V for a finger spacing of 30 µm.

		Finger Spacing = 30 µm						
Applied voltage bias (V)	***Sample***	t_{rise} **(s)**	t_{fall} **(s)**	I_{ph} **(mA)**	I_{dark} **(mA)**	I_{ph}/I_{dark} **(u.l)**	ΔI **(mA)**	R_{UV} **(A/W)**
1	***S1***	93	34	0.02	$1.1 \cdot 10^{-4}$	203	0.021	$8 \cdot 10^{-3}$
5	***S1***	174	88	1.34	$1.5 \cdot 10^{-2}$	89	1.3	0.5
10	***S1***	154	191	7.15	0.42	17	6.7	2.6

Annex G – ZnO and ZTO-based sensors exposed to different P_{UV}'s:

Figure G.1 a) and G.1 b) depicts the time-dependent photoresponse of ZnO and ZTO-based UV sensors, respectively, when exposed to different P_{UV}'s {0.05, 0.70, 1.70, 2.60, 3.50, 4.50 and 4.70 mW}, for the different tested finger spacings. The corresponding ΔI was extracted from these graphs and used to construct Figures 3.16 and 3.21 (introduced in the Results chapter). The graphs also demonstrate an increase in the I_{ph} produced with decreasing finger spacing, which in turn reflects in an increase in S_{UV}, as discussed in the Results chapter. It should be noted that the exposure area of the UV signal (A_o) was 0.15 cm^2 and the corresponding UV light intensities for the P_{UV} values used are as follows: (0.33, 4.78, 11.57, 17.38, 23.12, 29.78, 31.30 $mW \cdot cm^{-2}$).

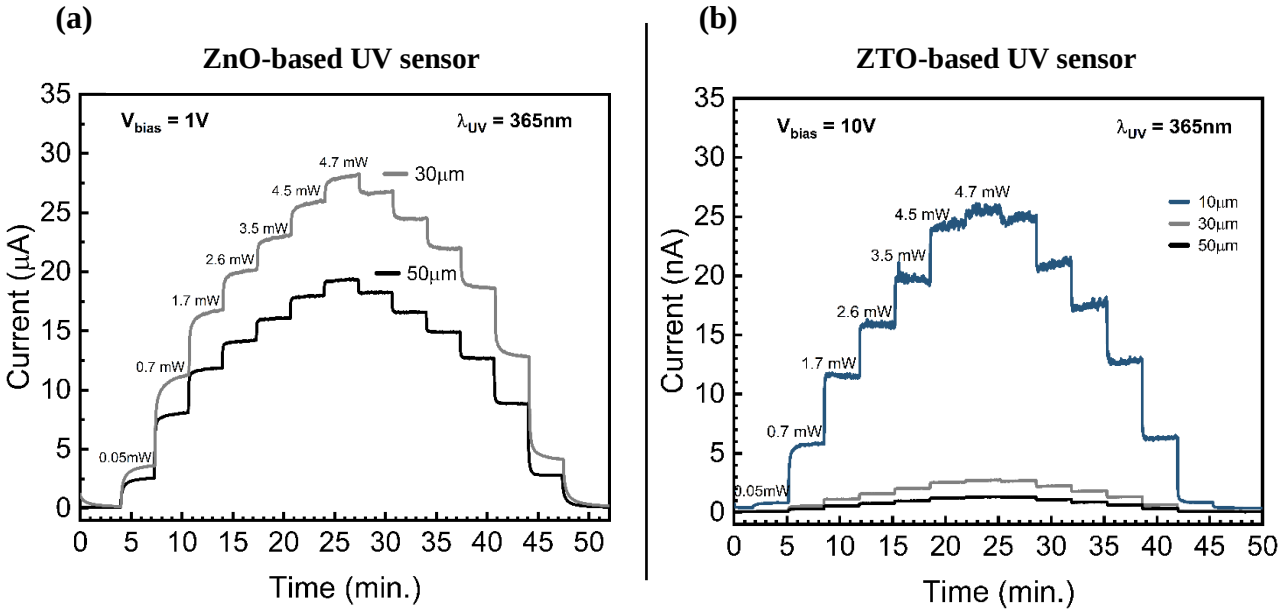

Figure G.1 : a) Time-dependent photoresponse of 30 and 50 µm ZnO-based UV sensors (a), and of 10, 30 and 50 µm ZTO-based UV sensors (b), when exposed to various P_{UV}'s for an applied voltage of 1V (a) and 10V (b), respectively.

Annex H – Finger Spacing influence on ZTO-based UV sensors under 5 V of applied voltage:

Figure H.1 illustrates the time-dependent photoresponse of ZTO-based UV sensors, including all finger spacings, under a voltage of 5 V. Additionally, Figure H.1 highlights that the sensor behavior, particularly its I_{ph}, stabilizes at 5 V, as evidenced by the absence of oscillations that were present in the 1 V tests.

Table H.1 presents a summary of the parameters extracted from Figure H.1 and demonstrates a comparable trend to the 10 V tests. The current-related parameters exhibit an increase with decreasing finger spacing, except for the I_{ph}/I_{dark}, which exhibited an initial increase during the transition from 50 to 30 µm, followed by a decrease from 30 to 10 µm. This difference distinguishes the 5 V tests from the 10 V tests, where the I_{ph}/I_{dark} always increased as the finger spacing decreased. The response times show a decrease in t_{rise} and a slight increase in the t_{fall}, again in agreement with the observations made in the 10 V tests.

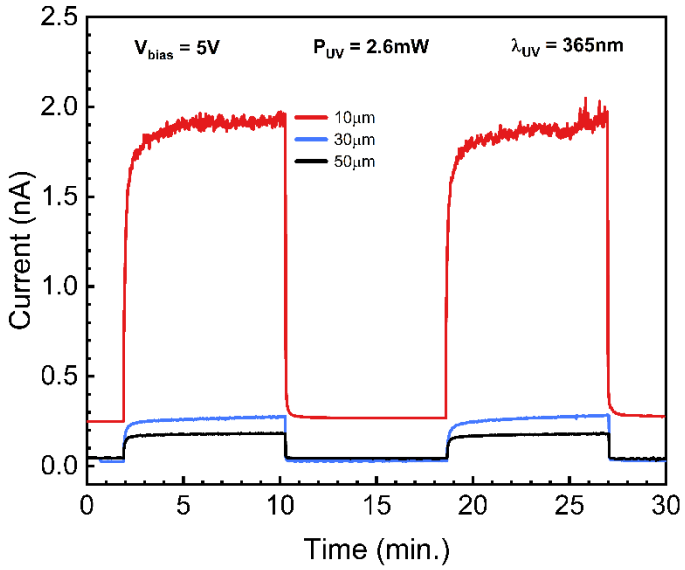

Figure H.1: ZTO-based UV sensor time-dependent photoresponse at a constant bias voltage of 5 V.

Table H.1: ZTO-based UV sensor parameters obtained as a function of finger spacing of 50, 30 and 10 µm at a fixed applied voltage of 5 V.

		5 V						
Finger Spacing (µm)	***Sample***	t_{rise} **(s)**	t_{fall} **(s)**	I_{ph} **(nA)**	I_{dark} **(nA)**	I_{ph}/I_{dark} **(n.l)**	ΔI **(nA)**	R_{UV} **(µA/W)**
50	***S1***	43	1.1	0.18	0.04	4	0.14	52
30	***S1***	91	1.4	0.28	0.03	9	0.25	98
10	***S1***	38	2.3	1.97	0.25	8	1.71	655

Annex I – Applied voltage influence on ZTO-based UV sensors with 30 and 50 µm of finger spacing:

Figure I.1(a) and (b) show the time-dependent photoresponse of ZTO-based UV sensors with finger spacings of 50 µm and 30 µm, respectively, under different applied voltages of 1, 5 and 10 V. The performance parameters of the sensors extracted from Figure I.1(a) and (b) are presented in Table I.1.

In the results chapter, the UV sensor with a finger spacing of 10 µm was selected for analysis. However, as shown in Table I.1, the effect of the applied voltage was similar for all three finger spacings studied (10, 30 and 50 µm). Regarding the response times, the t_{rise} increased significantly while the t_{fall} decreased slightly with increasing voltage. In addition, all other current-related parameters showed an increase with increasing applied voltage.

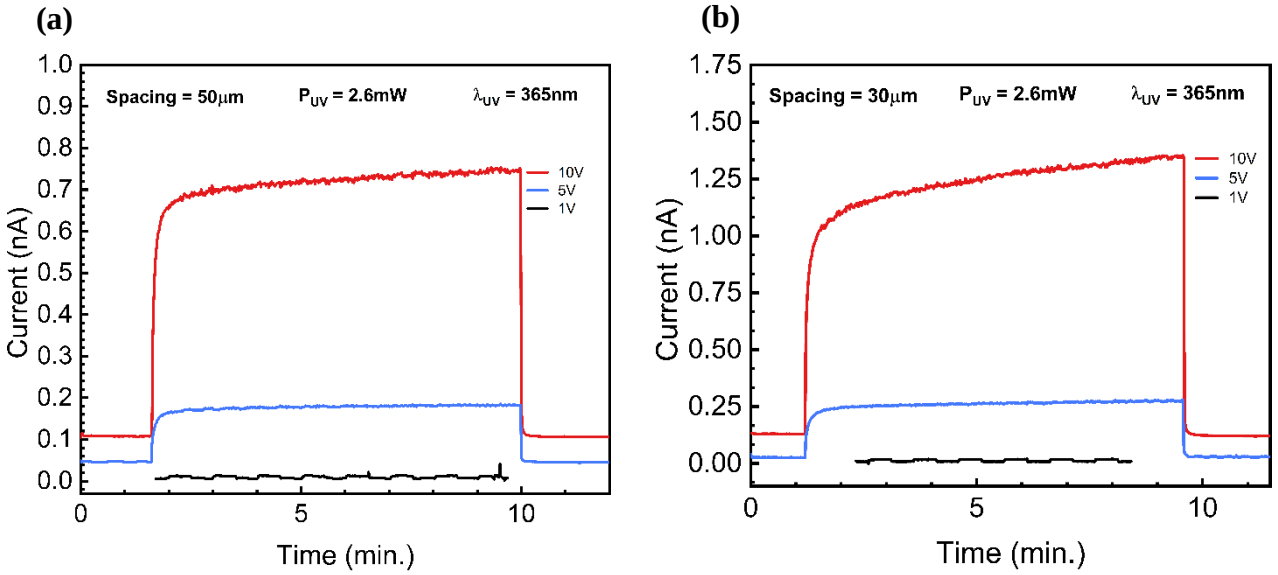

Figure I.1: Time-dependent photoresponse of ZTO-based UV sensors with finger spacings of 30 µm (a) and 50 µm (b) at different bias voltages of 1, 5, and 10 V.

Table I.1: ZTO-based UV sensor parameters obtained for 50 and 30 µm finger spacing sensors under 1, 5 and 10 V of applied voltage.

	Finger Spacing = 50 µm							**Finger Spacing = 30 µm**						
Applied voltage bias (V)	t_{rise} **(s)**	t_{fall} **(s)**	I_{ph} **(nA)**	I_{dark} **(nA)**	I_{ph}/I_{dark} **(u.l)**	ΔI **(nA)**	R_{UV} **(nA/W)**	t_{rise} **(s)**	t_{fall} **(s)**	I_{ph} **(nA)**	I_{dark} **(nA)**	I_{ph}/I_{dark} **(u.l)**	ΔI **(nA)**	R_{UV} **(nA/W)**
1	1	10	0.01	0.005	3	0.005	3	4	4.4	0.07	0.017	4	0.053	4
5	43	1.1	0.18	0.04	5	0.14	52	90	1.4	0.28	0.03	9	0.25	98
10	61	0.9	0.76	0.09	8	0.66	250	94	1.2	1.41	0.12	12	1.28	490

2023

DAVID MANUEL SEGURO DE CARVALHO

FABRICATION OF ULTRAVIOLET SENSORS BASED ON ZTO AND ZNO NANOWIRES

NOVA SCHOOL OF SCIENCE & TECHNOLOGY